Office of Naval Research Final Report

Reducing Noise from Single and Twin Supersonic Jets Using Very-Low-Frequency Control

(N00014-19-1-2431)

Professor Daniel J. Bodony (PI) and Sandeep R. Murthy
Department of Aerospace Engineering
University of Illinois at Urbana-Champaign

January 2024

1 Introduction

High speed jet noise from Naval tactical aircraft causes operational difficulties limiting communication between pilot and carrier deck crew, quickly damages deck crew hearing, and leads to sound-induced structural vibrations and fatigue. Several decades of experimental, theoretical, and computational investigations into the physics and control of jet noise have identified several important sound sources, including wavepackets (Jordan and Colonius, 2013), screech (Ponton and Seiner, 1992), Mach wave radiation (Williams and Maidanik, 1965), and broadband shock associated noise (Norum and Seiner, 1982). Reducing the loudest sources of jet noise, without sacrificing propulsive performance, has relied on intuition (Seiner et al., 2004), parametric survey (Bridges and Brown, 2004), or optimal control techniques (Kim et al., 2014).

A general and robust physics-based approach to jet noise reduction (JNR), that relies on the observation that coherent structures in turbulent jets strongly resemble instability wavepackets and considers the possibility that these coherent structures are governed by linear dynamics of small-amplitude fluctuations on a turbulent base-flow, is the focus of the current investigation. Many articles in the past (Michalke, 1977; Crighton and Gaster, 1976; Gudmundsson and Colonius, 2011) have considered the possibility that a linear model can faithfully reproduce the coherent turbulence structures in jet-like flows. These articles have been summarized in Jordan and Colonius (2013) and are shown to faithfully reproduce the observed spatial growth of coherent turbulence structures near the nozzle over a significant but limited range of frequencies. However, for the underlying theoretical model behind the linear analysis to be justified, the linear perturbations developing in the base flow must be deterministic in nature. Therefore, extending such a model to analyze chaotic nonlinear fluctuations around a statistical turbulent mean state has remained vague (Lesshafft et al., 2019).

A promising framework to understand turbulent jet noise is formulated by constructing a linearised Navier-Stokes system subject to stochastic forcing such that the statistical moments of the turbulent flow are governed by model equations (Farrell and Ioannou, 1993, 2019). Literature that investigates such a stochastic forcing applied to linearised Navier-Stokes equations predominantly focus on time-domain formulations of covariance dynamics; however, coherence in jet turbulence has often been analyzed in the frequency domain (Lesshafft et al., 2019). Specifically, spectral proper orthogonal decomposition (SPOD) has been used as a means to extract empirical coherent structures at a given frequency from numerical flow data (Garnaud et al., 2013; Lesshafft et al., 2019; Gudmundsson and Colonius, 2011). Recently linear stability analyses of jets has been carried out in a frequency-domain framework using optimal forcing/response structures (Garnaud et al., 2013). The forcing and response modes in this formalism are global in nature, and they are constructed as the singular modes of the global resolvent operator (Schmid, 2007). This analysis has been employed in the literature to model the stochastic dynamics of the Navier-Stokes equations (Sipp and Marquet, 2013). The work by Beneddine et al. (2016) demonstrates that the spatial structure of the optimal linear flow response agree with the leading SPOD modes, obtained from numerical simulations, and has established a formal justification for a direct comparison between optimal linear response structures and SPOD modes.

A crucial step in controlling turbulent jet flows is the selection and placement of an actuator-sensor pair. Historical evidence, intuition, hardware availability, or parametric optimization often influence these decisions. Alternatively, once a relevant definition of a base-flow is established, and it is recognized that small perturbations to non-normal operators (base-flow modifications) can result in substantial shifts to their eigenvalues (Chomaz, 2005; Natarajan et al., 2016a), an effective placement of an actuator-sensor pair can be identified. This will invariably be located in the region overlapped by the adjoint and forward eigenmodes of the system, also known as the wavemaker region. However, when essential dynamics of the flow cannot be captured by the eigenvalues of the governing non-normal linearized-compressible-Navier-Stokes operator, concepts such as eigenvalue sensitivity to base-flow modification need to be extended, as described in Brandt et al. (2011) and de Pando et al. (2014). These articles derive an analytical expression for the sensitivity of the optimal gain, with respect to base-flow modifications, and thus provide a means to evaluate the efficacy of a actuator-sensor pair capable of reducing the noise emanating from turbulent jet flows.

In this report, compressible large eddy simulations and resolvent analysis are used to achieve noise reduction in supersonic jets. Additionally, the report desribes current research towards extending linear-based JNR strategies to jets with strong shocks. Although such jets are common in high-performance aircraft, there is scant literature discussing forward and adjoint sensitivity analyses about flows with discontinuities in general, with even less prior work within the computational fluid dynamics realm. The question of how to address sensitivities with shock-laden flows follows a presentation of our progress, large-eddy simulation

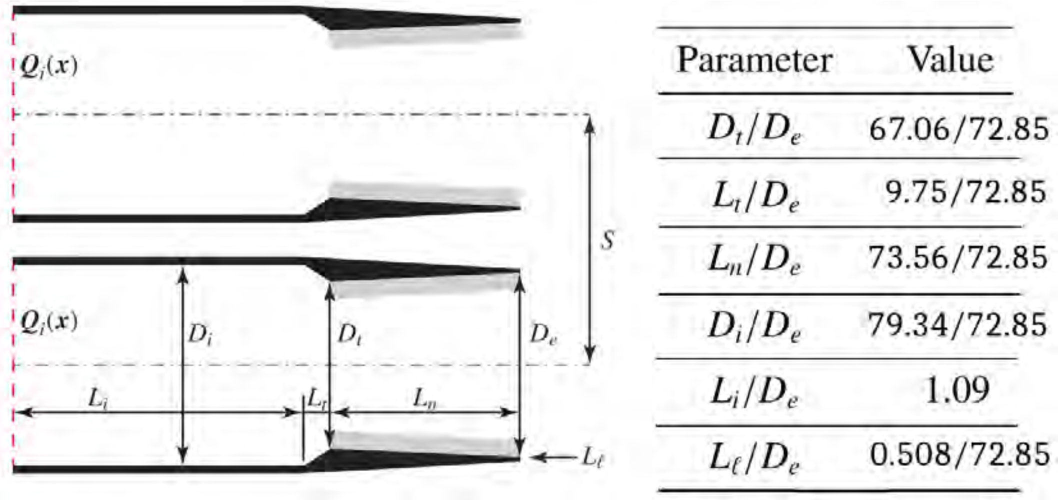

Parameter	Value
D_t/D_e	67.06/72.85
L_t/D_e	9.75/72.85
L_n/D_e	73.56/72.85
D_i/D_e	79.34/72.85
L_i/D_e	1.09
L_ℓ/D_e	0.508/72.85

Figure 1: Geometric details of single/twin conical converging-diverging nozzles.

framework and its application to underexpanded jets.

2 Project goal

The objective of the present work is to construct a resolvent framework, modified by the inclusion of an acoustic-output and hydrodynamic-input domain, to evaluate the sensitivity of the optimal gain, computed as per Brandt et al. (2011) and de Pando et al. (2014), with respect to base-flow modifications of a time-averaged turbulent jet flow, with the improvements suggested in Bodony and Natarajan (2012) and Natarajan et al. (2016b), to arrive at a tractable, yet, effective selection and placement of an actuator-sensor pair, capable of jet noise reduction, using linear feedback control.

2.1 Jet geometry and operating conditions

The generic jet geometry, shown in figure 1, consists of one or two identical conical converging-diverging nozzles issuing from an otherwise straight inflow section. The precise nozzle geometry is the same as that studied by NRL (Liu et al. (2013)). Although TACAIR nozzles have variable throat and exit areas this work focused on one area ratio of approximately 1.09, a design Mach number of 1.5 and corresponding fully expanded nozzle pressure ratio (NPR) of 3.7. The specific nozzle lengths are given in table accompanying the nozzle geometry presented in 1. When a twin configuration is used, the centerline-to-centerline spacing will be $S/D_e = 1.1$.

The $M_d = 1.5$ nozzle was run at the underexpanded NPR of 4.0 and the three temperature ratios of 1, 3 and 7. These conditions were studied computationally by NRL (Liu et al. (2021, 2013, 2016, 2017)) and the colder case experimentally at the University of Cincinnati (Munday et al. (2011); Liu et al. (2013)). The TTR = 3, NPR = 4 conditions for an isolated jet nozzle provides validation while the hotter isolated jets provided verification. The internal nozzle boundary layer is not included and instead a slip adiabatic wall boundary is considered. The inflow profile for each jet is specified purely in terms of the stagnation pressure and stagnation temperature at the nozzle inlet. The exit conditions of the jet nozzle are set by the ambient pressure boundary condition at the far-field boundaries.

2.2 Tasks

The research conducted is organized into tasks and documented below. All jets refer to the geometry and conditions given in the previous section.

Task 1 (Isolated jet prediction, validation and verification)

1. Implemented LES capability within the `PlasCom2` (Diener et al., 2019, 2017, 2020) compressible flow solver. The LES implementation uses a dynamic sub-grid-scale (SGS) model. It preserves fine scale turbulence and is capable of simulating strong-shocks with the help of a bandwidth-optimized hybrid-WENO scheme, that was developed in-house.

2. Implemented and verified the Ffowcs-Williams and Hawkings (FWH) surface integral method for far-field sound prediction.

3. Validated and verified unsteady three-dimensional large-eddy-simulations of an under-expanded turbulent jet at three different total temperature ratios (TTR $= 1$, 3 and 7). Here potential core length, centerline streamwise velocity, and far-field radiated sound were successfully compared with previous results from NRL (Liu et al. (2021, 2013, 2016, 2017)) and the University of Cincinnati (Munday et al. (2011); Liu et al. (2013)).

Task 2 (Single jet JNR development)

1. Implemented a tool to build linearized compressible Navier-Stokes (LCNS) operators, about a given base-flow, within the `PlasCom2` compressible flow solver. The solver is able to handle overset meshes whilst building a sparse operator, in parallel, using the PETSc software package.

2. Using our LCNS operator construction tool, optimal and sub-optimal resolvent modes corresponding to a given base-flow and Strouhal number were constructed. The computation of these modes incorporate input and output operators that select the region and type of perturbations that are of interest to the goal of JNR.

Task 3 (Single shock-free jet JNR testing)

1. Implemented and verified a base-flow-modification based linear-feedback-control, capable of JNR, in the `PlasCom2` compressible flow solver.

2. Resolvent analysis, described at the end of **Task 2**, helped discover the selection and placement of an actuator-sensor pair capable achieving JNR, through linear-feedback-control, in a subsonic axisymmetric jet issuing from a straight nozzle (to ensure shock-free flow). Thus providing a proof-of-concept of our physics based approach to JNR.

Task 4 (Single shock-laden jet JNR development)

1. Established conditions for a convergent numerical procedure capable of computing adjoint modes in shock-laden flows.
2. Derived a semi-analytical approach to compute viscous shock-laden resolvent modes. These semi-analytical results help evaluate the efficacy of a numerical procedure in computing resolvent modes about shock-laden base-flows. Thus establishing what an ideal numerical procedure for computing resolvent modes in shock-laden flows must converge to, with improving grid resolution.

Task 5 (Single shock-laden jet JNR testing)

1. **On going**: Apply the verified numerical procedure for resolvent mode computation, in the context of shock-laden base-flow, to the time averaged mean-flows from the single shock-laden jet simulations to obtain the appropriate selection and placement of an actuator-sensor pair capable achieving JNR.
2. **On going**: Demonstrate JNR on a single shock-laden jet emanating from a converging-diverging nozzle as shown in figure 1.

2.3 Outcomes

The primary outcome of the proposed effort is the application and evaluation of a resolvent informed linear-feedback-control, capable of reducing jet noise from supersonic jets. As a secondary outcome we have identified a semi-analytical approach to evaluate the efficacy of numerical methodologies to compute resolvent modes about shock-laden mean flows.

3 Large-Eddy Simulation Predictions of Jet Noise

This section describes the numerical implementation and application of our flow solver for simulating a 3D supersonic flow through a bi-conical tactical aircraft nozzle. Before describing how the LES capabilities are incorporated into our in-house compressible flow solver `PlasCom2`, we provide a brief summary of the solver's inherent capabilities.

3.1 Large-Eddy Simulation Methodology

`PlasCom2` solves the equations of mass, momentum, and energy conservation for a compressible, viscous fluid with an ideal gas equation of state, Fourier law of heat conduction and Newtonian viscous stresses

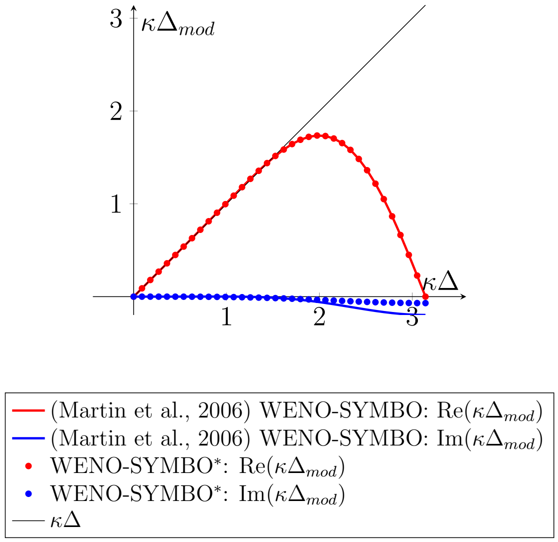

Figure 2: Bandwidth efficiency for the WENO-SYMBO and WENO-SYMBO* schemes.

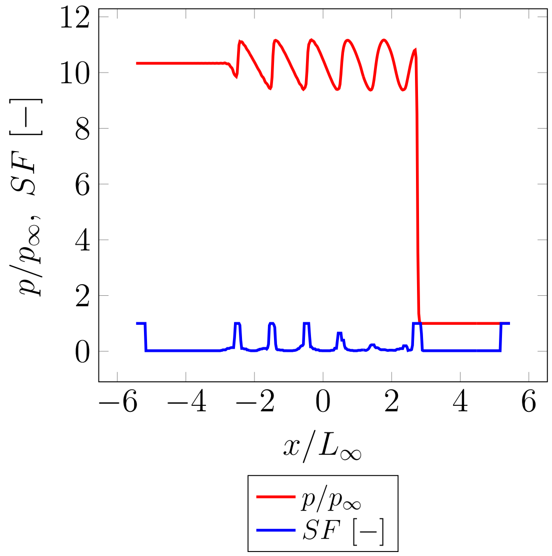

Figure 3: Switch function (SF) identifying the regions where WENO-SYMBO* is needed.

$\tau = \mu[\nabla \boldsymbol{u} + (\nabla \boldsymbol{u})^{\mathrm{T}}] + \lambda(\nabla \cdot \boldsymbol{u})\boldsymbol{I}$, where $\boldsymbol{I}$ is the identity tensor and $\boldsymbol{u}$ is the velocity field. The shear viscosity is temperature dependent and is modelled as $\mu/\mu_0 = (T/T_0)^{2/3}$. The equations are expressed in computational coordinates $\boldsymbol{\xi} = \boldsymbol{\Xi}(\boldsymbol{x})$, whose mapping $\boldsymbol{\Xi}$ to physical coordinates $\boldsymbol{x}$ of a mesh is one-to-one and onto Visbal and Gaitonde (2002). The solver has the ability to handle overset meshes (Bodony et al., 2011), whilst solving the non-dimensionalized compressible Navier-Stokes equations, in parallel, using a collocated finite difference approximation. The spatial derivatives are approximated by an author-modified WENO-SYMBO* scheme (to remove the long-time instability in Martín et al. (2006)), that are sixth order accurate in the interior. This scheme incorporates free-stream preservation as described in Nonomura et al. (2015) and bandwidth optimization as per a modified version of Martín et al. (2006) (see figure 2). The dynamic SGS model for compressible turbulence presented in Moin et al. (1991) is used to model the effect of the sub-grid scale dissipation on the unresolved yet represented scales of motion in the LES simulation. Repeated first derivatives are used to approximate the viscous terms and implementation of the boundary conditions uses the ghost cell approach.

3.1.1 Bandwidth optimized hybrid WENO scheme

This section describes the efforts made to improve the WENO-SYMBO scheme, as implemented in Martín et al. (2006), by retaining the bandwidth optimization they achieve, whilst removing the anti-dissipative behavior present in their implementation. Additionally, this section describes the form of hybrid-WENO-SYMBO that is now implemented in PlasCom2, to ensure that the new bandwidth optimized WENO scheme is applied only in the vicinity of flow-solution discontinuities.

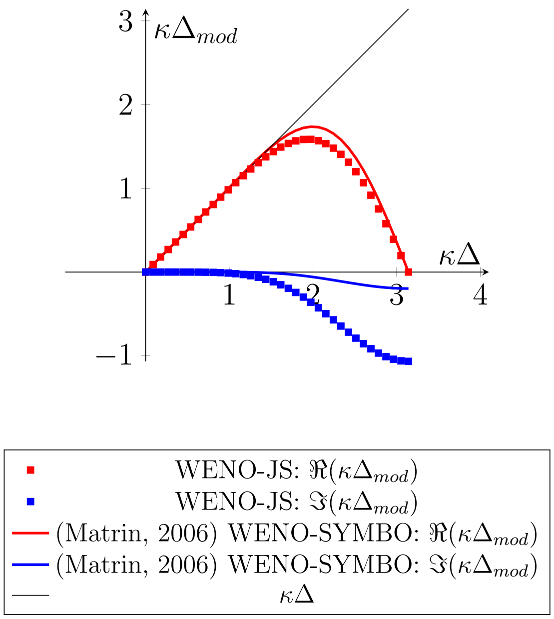

Figure 4: Bandwidth efficiency for the WENO-JS and WENO-SYMBO schemes.

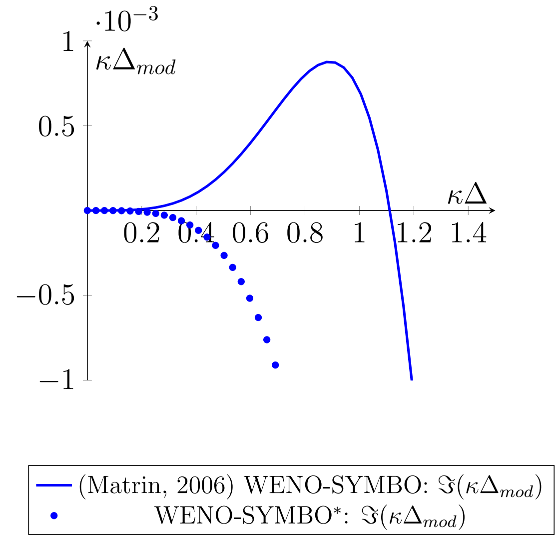

Figure 5: Anti-dissipative nature of WENO-SYMBO and how WENO-SYMBO* does not feature this issue.

Anti-dissipative behavior of the WENO-SYMBO scheme (Martín et al., 2006):

The WENO-SYMBO scheme, as per Martín et al. (2006), makes the following two modifications to the WENO-JS scheme by (Jiang and Shu, 1996). First, an additional candidate stencil is added such that the set of candidates is symmetric (SYM), rather than upwind-biased. The collection of stencils would now be symmetric, and thus the optimal weights would be theoretically capable of providing zero dissipation. And second, uses a bandwidth optimization (BO) process that maximizes a bandwidth-resolving efficiency index (Lele, 1992), to determine the weights for the optimal stencil, maintaining a small amount of dissipation at high wavenumbers, as shown in figure 4. However, whilst implementing this scheme we observed that this bandwidth efficiency plot, when studied carefully, revealed that in the vicinity of the wavenumber $\kappa\ \Delta x = \pi/3$, the imaginary component of the modified wavenumber is actually positive, as shown in figure 5, and this will lead to anti-dissipative behavior at these wavenumbers.

Modification to the WENO-SYMBO scheme that eliminates the anti-dissipative behavior:

We developed and tested a modification to the WENO-SYMBO scheme (WENO-SYMBO*) that involves a change in the integrated error function, which Martín et al. (2006) used to achieve a bandwidth optimization. This modification, ensures that the imaginary component of the modified wavenumber (featured in the bandwidth efficiency plots from figure 4 and 5) will be non-positive for all wavenumbers. Our modification to the integrated error function adds a constant dissipative bias ($C = 0.002$) across all wavenumbers as shown below

$$I = \int_0^{\pi} e^{\nu(\pi-\kappa\Delta)} \left(\sigma[\Re(\kappa\Delta_{mod}) - \kappa\Delta]^2 + (1-\sigma)\left[\Im(\kappa\Delta_{mod}) + C - \gamma \sin^{\mu}\left(\frac{\kappa\Delta}{2}\right)\right]^2 \right) d\kappa\Delta. \tag{1}$$

Table 1 summarizes the new optimal stencil weights corresponding to the WENO-SYMBO* scheme. This modification now ensures that the imaginary component of the modified wavenumber no longer features a region of positive dissipative-amplitude-error $\Im(\kappa\Delta_{mod})$, as shown in figure 5. Additionally, as seen in figure 2, the bandwidth efficiency is further improved when we compare the high wavenumber dissipative amplitude error $\Im(\kappa\Delta_{mod})$ values between the WENO-SYMBO and WENO-SYMBO* schemes.

Optimal stencil weights	WENO-SYMBO, (Martín et al., 2006)	WENO-SYMBO*
C_1	0.094647545896	0.0818335664489204
C_2	0.428074212384	0.4441518418703716
C_3	0.408289331408	0.3922117091318137
C_4	0.068988910311	0.0818028825488943

Table 1: New optimal stencil weights corresponding to the WENO-SYMBO* scheme.

Hybrid WENO:

The choice of symmetric stencils in the WENO-SYMBO* scheme helps reduce dissipation far from any flow-discontinuities. However, it was observed that even with these improvements the large eddy simulations of the decay of homogenous isotropic turbulence did not match the experimental observations presented in Comte-Bellot and Corrsin (1971). Thus, `PlasCom2` uses a hybrid scheme that selectively turns on WENO-SYMBO* only in the presence of flow-discontinuities. The flow-discontinuities are sensed using a shock sensor (switch function 6 from Li et al. (2017)) as shown in figure 3. The resulting scheme is able to simultaneously handle both shock-laden flows and does not adversely effect the cascade of energy from the large to the smallest scales of turbulence.

3.1.2 Dynamic sub-grid-scale model and explicit-filtering:

The dynamic SGS model for compressible turbulence presented in Moin et al. (1991) is used to model the effect of the sub-grid scale dissipation on the unresolved yet represented scales of motion in the LES simulation. This model computes the strain rate fields at two different scales (test and selective filters help acquire this information) and utilizes the spectral information in the large-scale field to extrapolate the small-scale stresses. The model then uses an algebraic identity derived by Germano et al. (1991) along with an eddy viscosity model to represent the SGS stresses at both scales. The expression derived for the eddy viscosity coefficient is both a function of space and time, and hence can be described as dynamic in nature. The coefficient can be negative in some regions and thus does not totally exclude backscatter, it provides for the proper asymptotic behavior of the stresses near the wall without ad-hoc damping functions, and it vanishes in laminar flow without ad-hoc intermittency functions. Explicit numerical methods for filtering that were developed, by Bogey and Bailly (2004), with the aim of computing flow and jet-noise with high accuracy and fidelity, are used in our LES implementation. Specifically, the filters SFo13p and TFo15p$_{(\pi/3)}$, from Bogey and Bailly (2004), are used for the selective and test filter, respectively.

3.2 LES verification

In this section, an accurate simulation of the decay of homogeneous isotropic turbulence is performed to verify the LES implementation.

This simulation uses the previously mentioned hybrid WENO scheme and dynamic SGS model to accurately simulate the cascade of energy from the large to the smallest scales of turbulence. Results from the large eddy simulations using this implementation are very encouraging and have been presented in figure 6. Here, the decay of turbulent kinetic energy and the expected 3D energy spectrum are compared to filtered experimental data from Comte-Bellot and Corrsin (1971).

3.3 Large Eddy Simulation Results

Using the optimized WENO-SYMBO* based shock capturing scheme, with a Ducros shock sensor, the shock-laden turbulent flow issuing from a biconical nozzle with nozzle pressure ratio ($\text{NPR} = p_0/p_\infty = 4$) have been simulated for a series three total temperature ratios ($\text{TTR} = T_0/T_\infty = 1, 3, 7$). Several simulation parameters are given in Tables 2 & 3. These specific parameters were chosen to allow for a direct comparison between the experimental and numerical results presented in Liu and Corrigan (2018) and Liu et al. (2013). The flow fields corresponding to the three different TTRs are shown, along with their corresponding sound fields, in figures 7 through 12. The flow is characterized by a strong shock cell pattern near the nozzle exit that initiates with a normal shock, as seen in the instantaneous Mach number contour plots. Observing the instantaneous pressure field perturbations it is observed that as the temperature increases, the mixing noise generation increases and Mach wave propagation dominates. Finally, it can be observed through the pressure field perturbation plots that the shock-associated acoustic waves propagate in both upstream and downstream directions.

Validation results concerning the case with $\text{TTR} = 1$ are summarized as follows. Figures 13 through 16 validate the LES based SPL calculations at certain spatial locations within the jet near-field (parallel to the jet axis), by demonstrating a faithful match with experimental data from Liu et al. (2013). The SPL data from the three TTR cases are compared at a single location $(\frac{z}{D_e}, \frac{r}{D_e}) = (10, 3.2)$ in figure 17. Figures 18 through 21 further strengthen trust in the LES predictions by demonstrating a faithful match between the LES simulation data from Liu and Corrigan (2018), both along the jet centerline and the jet-nozzle lipline.

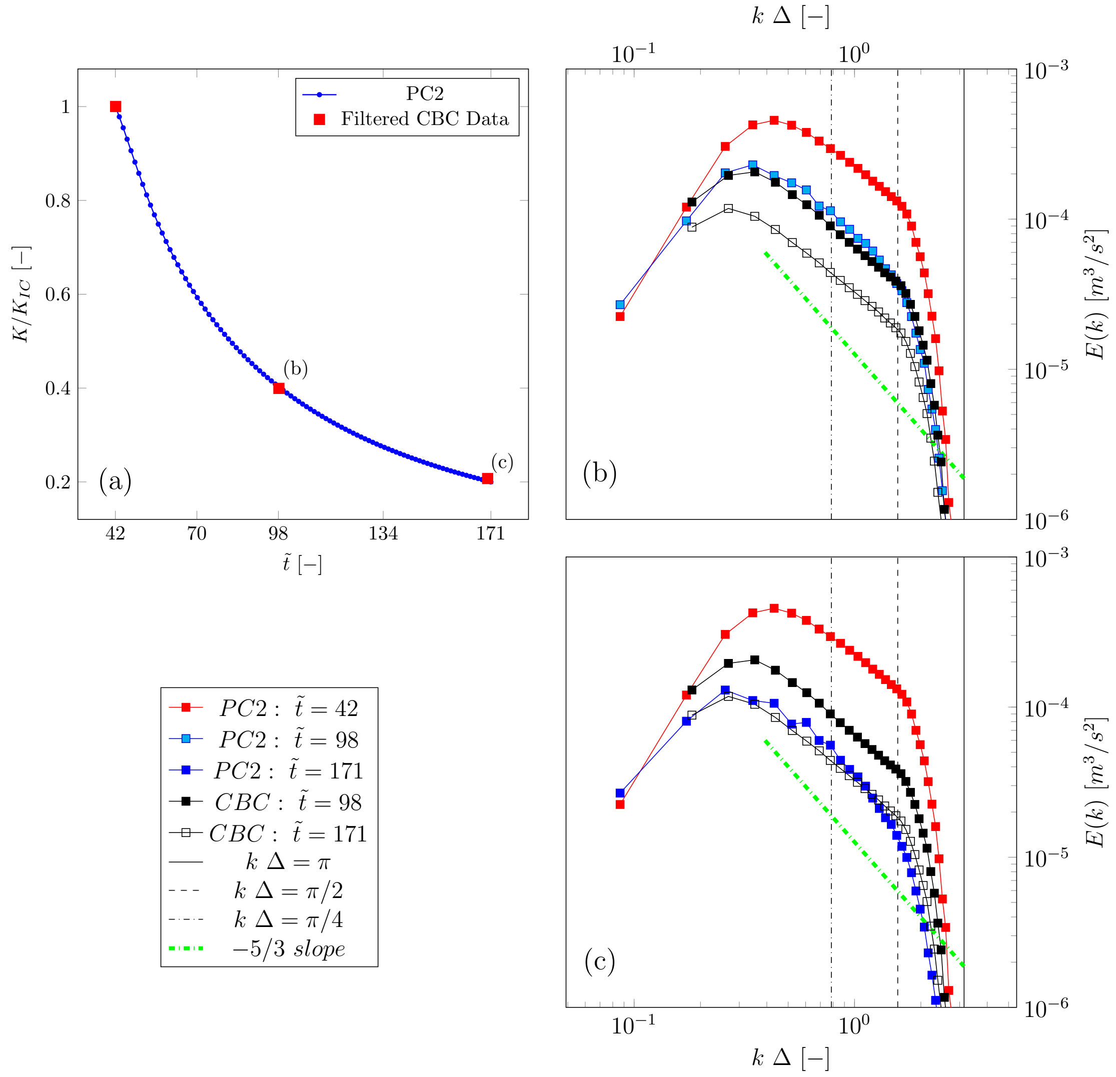

Figure 6: Large eddy simulation of the decay of homogenous isotropic turbulence and comparison against filtered experimental data from Comte-Bellot and Corrsin (1971). (a) Decay of turbulent kinetic energy verified against CBC experimental data. (b) 3D energy spectrum of the decay of homogeneous isotropic turbulence at 98 non-dimensional time units. (c) 3D energy spectrum of the decay of homogeneous isotropic turbulence at 171 non-dimensional time units

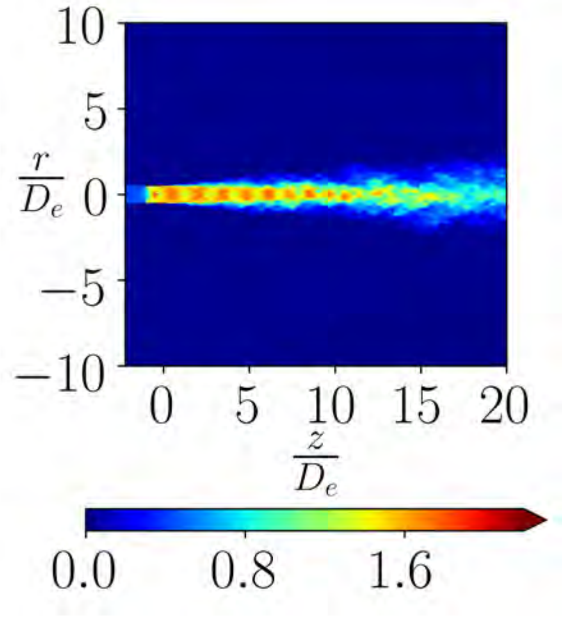

Figure 7: Instantaneous Mach number for NPR = 4, TTR = 1 jet.

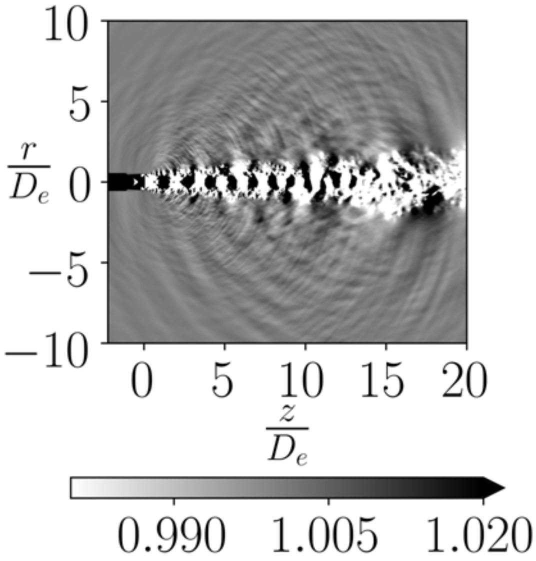

Figure 8: Instantaneous pressure field for NPR = 4, TTR = 1 jet.

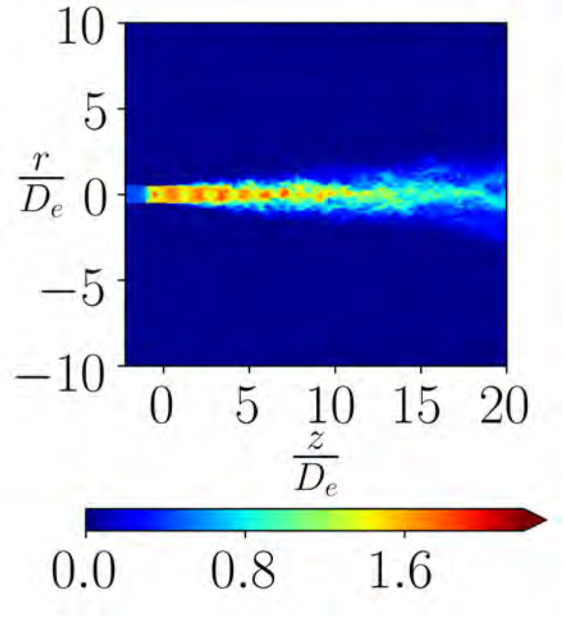

Figure 9: Instantaneous Mach number for NPR = 4, TTR = 3 jet.

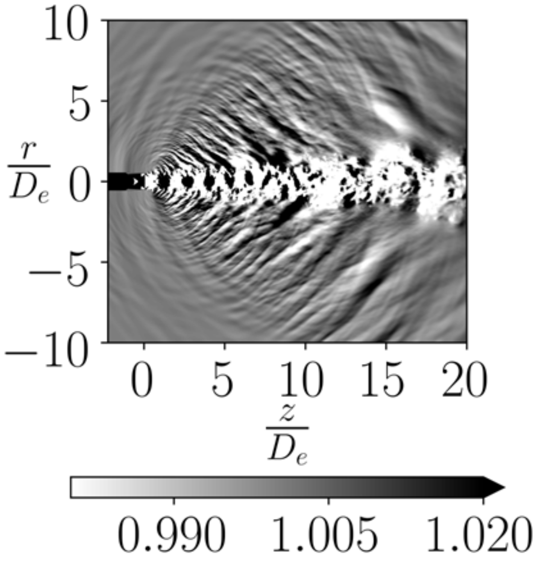

Figure 10: Instantaneous pressure field for NPR = 4, TTR = 3 jet.

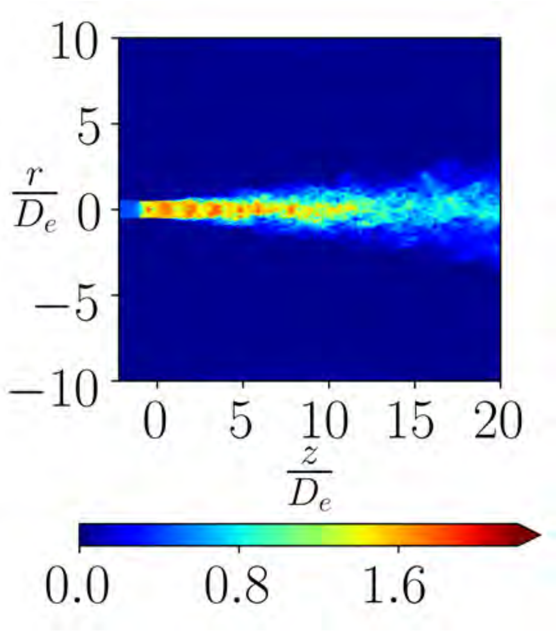

Figure 11: Instantaneous Mach number for NPR = 4, TTR = 7 jet.

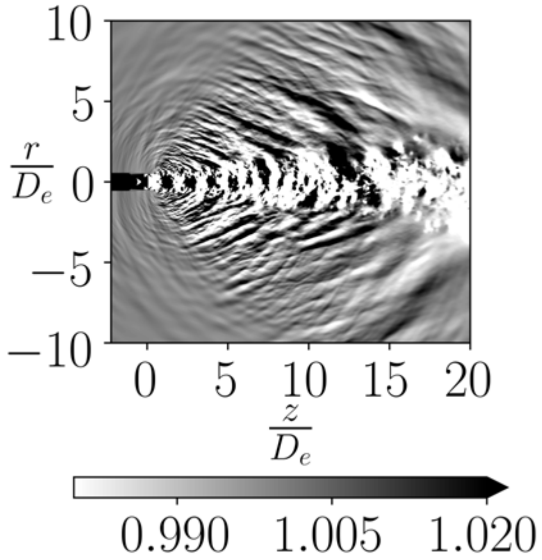

Figure 12: Instantaneous pressure field for NPR = 4, TTR = 7 jet.

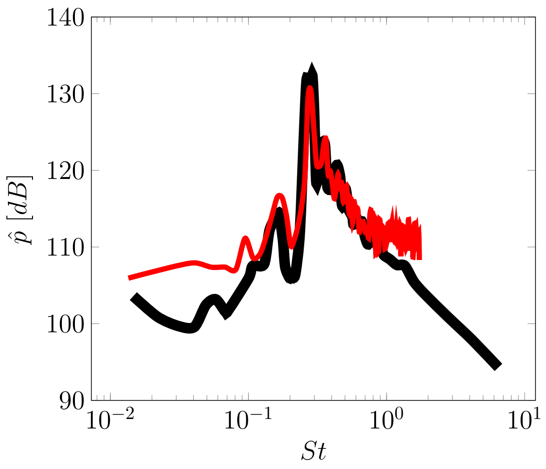

Figure 13: TTR = 1, NPR = 4, `plascom2x` LES simulation based SPL calculation at $(\frac{z}{D_e}, \frac{r}{D_e}) = (0, 1.5)$ (represented by 🟥) compared against experimental data (represented by ⬛) from Liu et al. (2013).

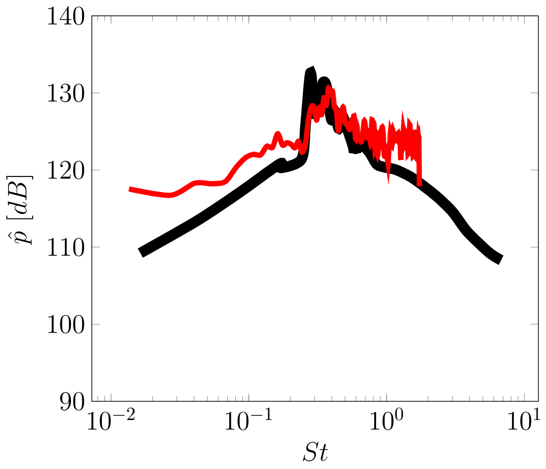

Figure 14: TTR = 1, NPR = 4, `plascom2x` LES simulation based SPL calculation at $(\frac{z}{D_e}, \frac{r}{D_e}) = (5, 2.3)$ (represented by 🟥) compared against experimental data (represented by ⬛) from Liu et al. (2013).

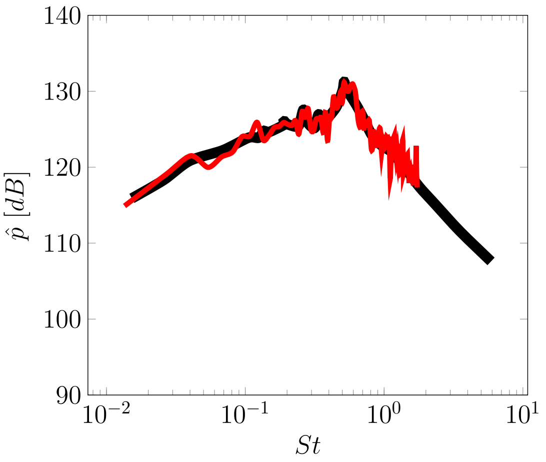

Figure 15: TTR = 1, NPR = 4, `plascom2x` LES simulation based SPL calculation at $(\frac{z}{D_e}, \frac{r}{D_e}) = (10, 3.2)$ (represented by 🟥) compared against experimental data (represented by ⬛) from Liu et al. (2013).

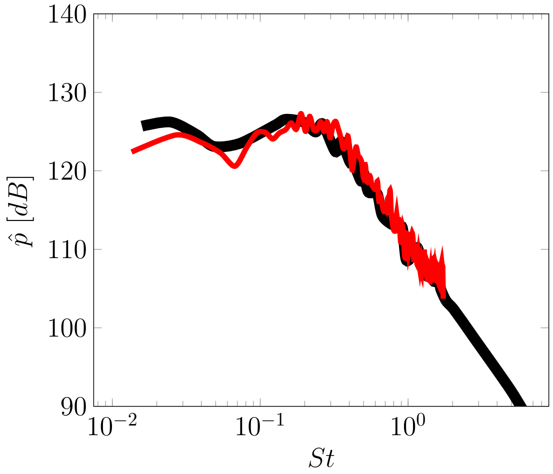

Figure 16: TTR = 1, NPR = 4, `plascom2x` LES simulation based SPL calculation at $(\frac{z}{D_e}, \frac{r}{D_e}) = (20, 4.8)$ (represented by 🟥) compared against experimental data (represented by ⬛) from Liu et al. (2013).

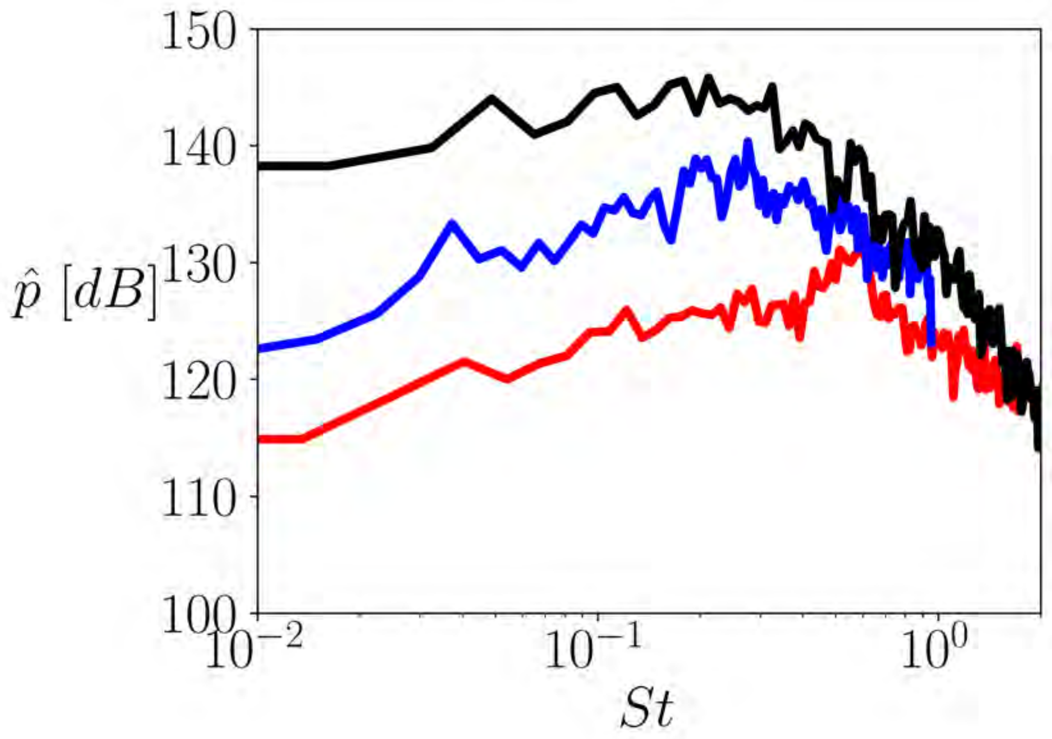

Figure 17: TTR = 1 (red), 3 (blue) and 7 (black), NPR = 4, `plascom2x` LES simulation based SPL calculations at $(\frac{z}{D_e}, \frac{r}{D_e}) = (10, 3.2)$ are compared to indicate the effect of jet temperature on jet noise.

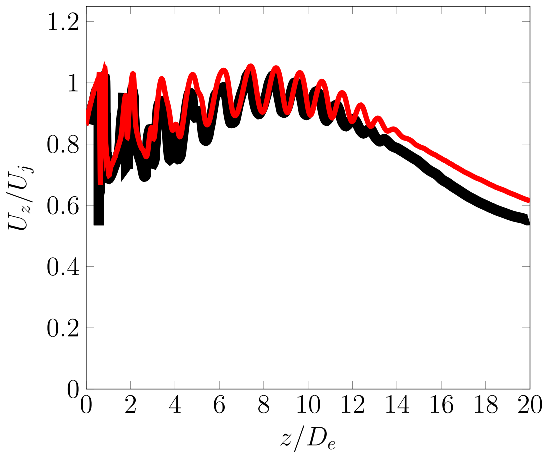

Figure 18: TTR = 1, NPR = 4, `plascom2x` based center-line axial velocity (represented by 🟥) comparison against the slip wall (no boundary layer) LES simulation data (represented by ⬛) from Liu and Corrigan (2018).

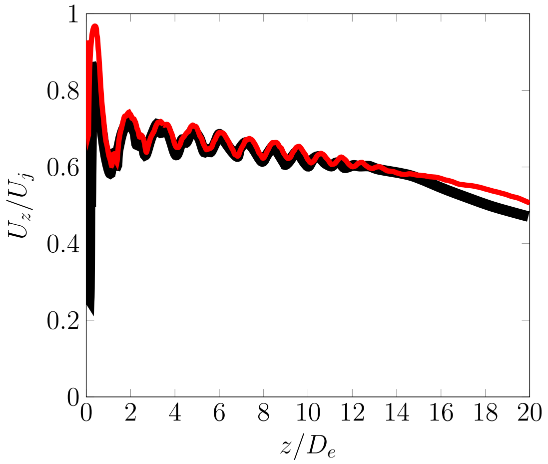

Figure 19: TTR = 1, NPR = 4, `plascom2x` based lip-line axial velocity (represented by 🟥) comparison against slip wall (no boundary layer) LES simulation data (represented by ⬛) from Liu and Corrigan (2018).

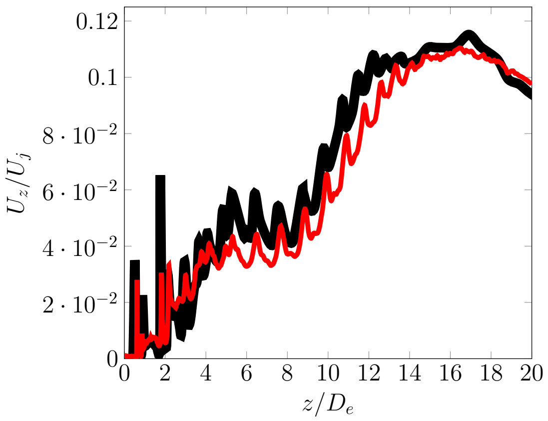

Figure 20: TTR = 1, NPR = 4, `plascom2x` based center-line axial turbulence intensity (represented by 🟥) comparison against slip wall (no boundary layer) LES simulation data (represented by ⬛) from Liu and Corrigan (2018).

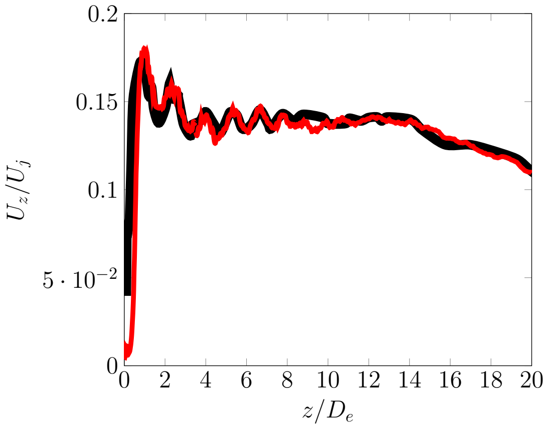

Figure 21: TTR = 1, NPR = 4, `plascom2x` based lip-line axial turbulence intensity (represented by 🟥) comparison against slip wall (no boundary layer) LES simulation data (represented by ⬛) from Liu and Corrigan (2018).

Table 2: Simulation parameters for the 3D bi-conical nozzle compressible LES jet simulation.

Domain size	$(L_z, L_r) = (62D_e, 15D_e)$
Grid points mesh 1	$(N_{z,1}, N_{r,1}, N_{\theta,1}) = (70, 231, 300)$
Grid points mesh 2	$(N_{z,2}, N_{r,2}, N_{\theta,2}) = (73, 593, 300)$
Grid points mesh 3	$(N_{z,3}, N_{r,3}, N_{\theta,3}) = (126, 895, 129)$
Grid points mesh 4	$(N_{z,4}, N_{r,4}, N_{\theta,4}) = (129, 1098, 129)$
Grid points mesh 5	$(N_{z,5}, N_{r,5}, N_{\theta,5}) = (196, 1460, 300)$
Nozzle geometry details	See figure 1
Reynolds number	$\rho_\infty \; c_\infty R/\mu_\infty = 3.9 \times 10^6$
Nozzle exit Mach number	1.5
Total Temperature Ratio (TTR)	$T_{o,in}/T_\infty = 1.0$
Nozzle Pressure Ratio (NPR)	$p_{o,in}/p_\infty = 4.0$

Table 3: Simulation details common to all simulations

Prandtl number (Pr)	0.71
γ	1.4
R_{gas}	287.05 $[m^2 s^{-2} K^{-1}]$
C_p	1004.675 $[m^2 s^{-2} K^{-1}]$
Power viscosity model (A, *power*)	$(1, 2/3)$
Wall boundary condition	Adiabatic slip wall

4 Linear analysis based Jet Noise Reduction

The linear analysis about the jet mean flow to support JNR are also performed using our in-house code `PlasCom2`. The construction of the linearized Navier–Stokes operator ($\boldsymbol{L}$), used for the global linear stability analysis of the jets, is as shown below (in Matlab-like notation):

$$\boldsymbol{L}(: \;, \; i) = \frac{\tilde{\boldsymbol{R}}(\boldsymbol{Q} + \epsilon \; \boldsymbol{e_i}) - \tilde{\boldsymbol{R}}(\boldsymbol{Q})}{\epsilon}, \tag{2}$$

where, $\epsilon = 10^{-8}$, the vector $\boldsymbol{e_i}$ is a unit vector with a 1 in the ith position, $\boldsymbol{Q}$ is the vector of unknowns and $\tilde{\boldsymbol{R}}$ is the discretized right-hand side of the non-linear compressible Navier-Stokes equations, including the WENO-SYMBO* terms, sponges and ghost boundary points, which accepts the state ($\boldsymbol{Q}$) or its perturbed form ($\boldsymbol{Q} + \epsilon \; \boldsymbol{e_i}$) as input. The next section briefly describes several aspects of the linear analysis, performed as a part of this research effort, such as modal analysis, resolvent analysis and structural sensitivity analysis.

4.1 Modal analysis

The discretized flow equations may be written as

$$\frac{d\boldsymbol{Q}}{dt} = \tilde{\boldsymbol{R}}(\boldsymbol{Q}). \tag{3}$$

Linearization of Eq. (3) for small perturbations $\boldsymbol{Q}' = \boldsymbol{Q} - \bar{\boldsymbol{Q}}$ to the base-flow $\bar{\boldsymbol{Q}}$ yields

$$\frac{d\boldsymbol{Q}'}{dt} = \boldsymbol{L}(\bar{\boldsymbol{Q}})\ \boldsymbol{Q}' \tag{4}$$

where $\boldsymbol{L}$ is the discrete right hand side operator evaluated about the axisymmetric base-flow $\bar{\boldsymbol{Q}}$. The eigenvalue problem considered is based on a modal decomposition of the form

$$\boldsymbol{Q}' = \hat{\boldsymbol{Q}}(r, z)\ e^{im\theta + i\omega t} \tag{5}$$

where m is the specified azimuthal mode number and ω is the sought-after eigenvalue with eigenmode $\hat{\boldsymbol{Q}}$. Now, Eq. (4) is cast as an eigenvalue problem, as shown below, and can be solved to obtain the modal solutions corresponding to the base-flow $\boldsymbol{Q}$,

$$\boldsymbol{L}\hat{\boldsymbol{Q}} = i\omega\hat{\boldsymbol{Q}}. \tag{6}$$

4.2 Resolvent analysis

The modal analysis solutions are sufficient to investigate the stability of a given base-flow at large times. The least stable among the flow eigenvalues provides this information. However, even stable flows can undergo significant perturbation energy growth owing to the non-normality of the linearized Navier-Stokes equations. To assess the energy growth of stable flows, a non-modal or input-output approach is therefore required (Schmid et al., 2002). This type of analysis attempts to characterize the non-normality of the governing operator, in the frequency domain, by finding the largest possible response of the system to time-periodic forcing (Farrell and Ioannou, 1996; Jovanović and Bamieh, 2005). The goal of this analysis is to quantify energy amplifications in the flow. To achieve this we begin with the linear input-output system formed by rewritting the discretized flow equations (3) in the following form

$$\frac{d\boldsymbol{Q}'}{dt} = \boldsymbol{L}(\bar{\boldsymbol{Q}})\ \boldsymbol{Q}' + \boldsymbol{B}\ \boldsymbol{f}, \quad \& \quad \boldsymbol{r} = \boldsymbol{C}\ \boldsymbol{Q}', \tag{7}$$

where the vector $\boldsymbol{f}$ contains zero-mean source terms of the continuity, momentum and energy equations, and represents an external forcing on the linearized-compressible-Navier-Stokes equations. The vector $\boldsymbol{r}$ represents the vector holding the quantity of interest, that is, the far-field pressure fluctuations. And, the matrices $\boldsymbol{B}$ and $\boldsymbol{C}$ specify the inputs-to (state vector fluctuations close to the nozzle, Jeun et al. (2016)) and outputs-from (far-field pressure fluctuations, Jeun et al. (2016)) the resolvent analysis that help reveal the influence of the jet on the far-field acoustics.

A Fourier-transformation of the above equations, in the form

$$\boldsymbol{r}(\boldsymbol{x},t) = \int_{\infty}^{-\infty} \hat{\boldsymbol{r}}(\boldsymbol{x},\omega) e^{i\omega t} d\omega, \qquad \boldsymbol{Q}'(\boldsymbol{x},t) = \int_{\infty}^{-\infty} \hat{\boldsymbol{Q}}(\boldsymbol{x},\omega) e^{i\omega t} d\omega, \qquad \boldsymbol{f}(\boldsymbol{x},t) = \int_{\infty}^{-\infty} \hat{\boldsymbol{f}}(\boldsymbol{x},\omega) e^{i\omega t} d\omega, \tag{8}$$

yields a frequency domain system

$$\hat{\boldsymbol{r}} = \boldsymbol{C}\ \hat{\boldsymbol{Q}} = \boldsymbol{C}\ (i\omega \boldsymbol{I} - \boldsymbol{L})^{-1}\ \boldsymbol{B}\ \hat{\boldsymbol{f}}\ =\ \boldsymbol{C}\ \boldsymbol{R}(\omega)\ \boldsymbol{B}\ \hat{\boldsymbol{f}}\ =\ \boldsymbol{H}(\omega)\ \hat{\boldsymbol{f}}, \tag{9}$$

where $\boldsymbol{R}(\omega)$ is the resolvent operator (Schmid, 2007) and $\boldsymbol{H}(\omega)$ is the frequency domain input-output operator relating the input and output modes. Furthermore, the input $\boldsymbol{f}$ can represent all terms nonlinear in $\boldsymbol{Q}'$, therefore a forcing with its Fourier-transform $\hat{\boldsymbol{f}}$ induces an inherent coupling between all frequencies. In order to make use of the system (9) for the purpose of modelling, a closure assumption is required that allows a decoupling of frequencies. However, following previous efforts in literature (Lesshafft et al., 2019), $\boldsymbol{f}$ is regarded as a stochastic forcing term and neglect the dependence of $\hat{\boldsymbol{f}}$, at one given frequency, on $\hat{\boldsymbol{r}}$ at other frequencies.

Now, defining the norm used to measure the input and output mode energy as shown below

$$||\hat{\boldsymbol{r}}||^2\ =\ \hat{\boldsymbol{r}}^H\ \boldsymbol{D}_r\ \hat{\boldsymbol{r}}\ =\ \hat{\boldsymbol{r}}^H\ \boldsymbol{N}_r^H\ \boldsymbol{N}_r\ \hat{\boldsymbol{r}}, \tag{10}$$

$$||\hat{\boldsymbol{f}}||^2\ =\ \hat{\boldsymbol{f}}^H\ \boldsymbol{D}_f\ \hat{\boldsymbol{f}}\ =\ \hat{\boldsymbol{f}}^H\ \boldsymbol{N}_f^H\ \boldsymbol{N}_f\ \hat{\boldsymbol{f}}, \tag{11}$$

an expression for the gain between input and output energy can be formulated as

$$\sigma^2 = \frac{||\hat{\boldsymbol{r}}||^2}{||\hat{\boldsymbol{f}}||^2} = \frac{\hat{\boldsymbol{f}}^H\ \boldsymbol{H}^H(\omega)\ \boldsymbol{N}_r^H\ \boldsymbol{N}_r\ \boldsymbol{H}(\omega)\ \hat{\boldsymbol{f}}}{\hat{\boldsymbol{f}}^H\ \boldsymbol{N}_f^H\ \boldsymbol{N}_f\ \hat{\boldsymbol{f}}} = \frac{\hat{\boldsymbol{f}}^H\ \boldsymbol{N}_f^H\ \boldsymbol{N}_f^{-H}\ \boldsymbol{H}^H(\omega)\ \boldsymbol{N}_r^H\ \boldsymbol{N}_r\ \boldsymbol{H}(\omega)\ \boldsymbol{N}_f^{-1}\ \boldsymbol{N}_f\ \hat{\boldsymbol{f}}}{\hat{\boldsymbol{f}}^H\ \boldsymbol{N}_f^H\ \boldsymbol{N}_f\ \hat{\boldsymbol{f}}}, \tag{12}$$

The expression for gain in equation (12) can be viewed as a Rayleigh quotient, involving the Hermitian operator $\boldsymbol{N}_f^{-H}\ \boldsymbol{H}^H(\omega)\ \boldsymbol{N}_r^H \boldsymbol{N}_r\ \boldsymbol{H}(\omega)\ \boldsymbol{N}_f^{-1}$. In other words, σ is equal to the largest singluar value of the operator $\boldsymbol{N}_r\ \boldsymbol{H}(\omega)\ \boldsymbol{N}_f^{-1} = \boldsymbol{U\Sigma V}^H$ and the forcing and response structures that feature the largest gains are given by $\boldsymbol{\hat{f}_i = N_f^{-1}\hat{v}_i}$ ($\boldsymbol{\hat{v}_i}$ are columns of $\boldsymbol{V}$) and $\boldsymbol{\hat{r}_i = \sigma_i N_r^{-1} \hat{u}_i}$ ($\boldsymbol{\hat{u}_i}$ are columns of $\boldsymbol{U}$ and σ_i are the corresponding singular values), respectively.

To further specify the nature of the far-field pressure fluctuations that the input-output analysis must pay attention to, we integrate the Ffowcs Williams–Hawkings (FWH) surface method into the resolvent analysis procedure. The operator $\boldsymbol{C}$ is multiplied by a new operator $\boldsymbol{F}$, that represents a linearized version of the FWH surface method (Mendez et al., 2009) acting on the near-field pressure, to produce the operator $\boldsymbol{C}_{\text{modified}}\ =\ \boldsymbol{FC}$. Thus, the linearized FWH far-field estimation procedure is embedded into this new output operator C_{modified} and enables the SVD procedure mentioned above to find the optimal forcing structures within the jet plume which feature the largest non-normal response (σ) in terms of far-field pressure disturbances/noise. The linearized form of the FWH procedure (Mendez et al., 2009) is given in the equations below

$$\hat{p}(\boldsymbol{x},\omega) = \int_S \left(\hat{p}(\boldsymbol{y},\omega) \frac{\partial \hat{G}_c(\boldsymbol{x},\boldsymbol{y})}{\partial y_i} - \hat{G}_c(\boldsymbol{x},\boldsymbol{y}) \frac{\partial \hat{p}(\boldsymbol{y},\omega)}{\partial y_i} \right) n_i(\boldsymbol{y}) dS(\boldsymbol{y}), \tag{13}$$

where $\hat{p}$ is the time-Fourier-transformed/frequency-domain pressure field and the expression for the frequency domain convected Green's function $\hat{G}_c$ is given below,

$$\hat{G}_c(\boldsymbol{x},\boldsymbol{y}) = \exp\left((i\ \omega\ r_g - i\ \omega\ M(x_1 - y_1)) / (\beta^2 c_\infty) \right) / (4\pi r_g), \tag{14}$$

where, $r_g = \left((x_1 - y_1)^2 + \beta^2 (x_2 - y_2)^2 + \beta^2 (x_3 - y_3)^2 \right)^{1/2}$, $\beta^2 = 1 - M^2$ and the mean flow has a Mach number $M = U_\infty / c_\infty$ and directed along the x axis. Since the above expression for $\hat{p}(\boldsymbol{x},\omega)$ is linear it can be represented as a matrix operator $\boldsymbol{F}$ that acts on near-field pressure ($\boldsymbol{CQ'}$) in the linear regime of the flow-solution (in other words $\boldsymbol{C}_{\text{modified}} = \boldsymbol{FC}$).

4.3 Structural sensitivity analysis

The resolvent modes, described in the previous section, can further be utilized to develop a control strategy using co-located linear feedback (Bodony and Natarajan, 2012; Natarajan et al., 2016b), where the feedback sensing is based on the difference between the instantaneous value of the state variables from that of a RANS or time-averaged base-flow.

The discretized flow equations, as in equation (3), with the co-located linear-feedback-control, are as shown below

$$\frac{d\boldsymbol{Q}}{dt} = \tilde{R}(\boldsymbol{Q}) + \underbrace{\alpha \boldsymbol{C}(\boldsymbol{Q} - \bar{\boldsymbol{Q}})}_{\text{Control } \boldsymbol{F}(\boldsymbol{x},t)} = \boldsymbol{L}(\bar{\boldsymbol{Q}})\ \boldsymbol{Q}' + H.O.T + \underbrace{\alpha \boldsymbol{C}\boldsymbol{Q}'}_{\text{Control } \boldsymbol{F}(\boldsymbol{x},t)}, \tag{15}$$

where $\boldsymbol{Q} \equiv (\rho, \rho u, \rho v, \rho w, \rho E)$, α is the control gain which is a free parameter that can be varied to change the strength of the control and $\boldsymbol{C}$ is a Gaussian supported control matrix designed to alter the non-modal response of the linearized operator $\boldsymbol{L(\bar{Q})}$, such that, the gain experienced by input disturbances within the jet plume, capable of affecting the output far-field acoustics, is reduced. The exact form of the matrix $\boldsymbol{C}$ is given below

$$\boldsymbol{C} = \underbrace{\begin{bmatrix} 0 & 0 & 0 & 0 & 0 \\ 0 & 0 & 0 & 0 & 0 \\ 0 & 0 & 0 & 0 & 0 \\ 0 & 1 & 0 & 0 & 0 \\ 0 & 0 & 0 & 0 & 0 \end{bmatrix}}_{\tilde{\boldsymbol{C}}} e^{\left(-(x-x_0)^2/\ell_x^2\ -\ (y-y_0)^2/\ell_y^2\ -\ (z-z_0)^2/\ell_z^2 \right)}, \tag{16}$$

where (x_0, y_0, z_0) is the center of the actuator and, ℓ_x, ℓ_y and ℓ_z are the support terms in the x, y and z directions, respectively. Additionally, matrix $\tilde{\boldsymbol{C}}$ shows an example of how forcing may be applied to the evolution of the term ρw using feedback/input from terms corresponding to ρu in the perturbation state vector $\boldsymbol{Q}' = \boldsymbol{Q} - \bar{\boldsymbol{Q}}$.

Next, a discrete structural sensitivity analysis gives an estimate of the change in gain ($d\sigma$), due to the linear-feedback-control described in equation (15), for values of α that would allow the matrix $\alpha\boldsymbol{C}$ to be viewed as a perturbation $d\boldsymbol{L}$ to the operator $\boldsymbol{L}(\bar{\boldsymbol{Q}})$ in the linear limit

$$d\sigma \approx Re\left(\hat{\boldsymbol{u}}^H(\boldsymbol{N}_r\boldsymbol{C}\ (\boldsymbol{R}\ d\boldsymbol{L}\ \boldsymbol{R})\ \boldsymbol{B}\boldsymbol{N}_f^{-1})\ \hat{\boldsymbol{v}}/(\hat{\boldsymbol{u}}^H\hat{\boldsymbol{u}})\right). \tag{17}$$

The objective is to optimize the movement of the chosen target singular value. The optimization seeks, for the case of gain (σ) minimization, the solution

$$\boldsymbol{C}^* \equiv \underbrace{\text{argmin}}_{\boldsymbol{C},||\tilde{\boldsymbol{C}}||}\ \text{Re}\left(\alpha^{-1}d\sigma\right), \tag{18}$$

with respect to the parameters $\left\{\tilde{\boldsymbol{C}}, x_0, y_0, z_0, \ell_x, \ell_y, \ell_z\right\}$.

4.4 Resolvent analysis verification

This verification is set up in order to reproduce the results published in Jeun et al. (2016) and help verify the current implementation. In the sub-sections that follow the nature of the axisymmetric RANS mean-flow solution and its non-modal behavior, resulting from the linearized FWH surface method augmented resolvent analysis, are described.

4.4.1 Flow solution

The simulation parameters, of an axisymmetric RANS simulation of supersonic flow through a straight nozzle (with radius R), are summarized in Tables 4 and 5. The stretched computational grid used $(N_z, N_r) = (721, 141)$ points in the axial and radial directions, respectively, and was shown to be sufficiently refined in Jeun et al. (2016). Figure 22 shows a line plot of its centerline axial velocity, which includes a verification against data from Jeun et al. (2016). The mean-flow solution $\bar{\boldsymbol{Q}}$, that was used to create figure 22, was solved for using an in-house modified version of OpenFOAM-8, capable of incorporating the correct axisymmetric flow corrections into a RANS simulation, using the standard k-ϵ model. For the RANS calculation, an initial flow solution, corresponding to an inlet Mach number of 1.5, total temperature ratio TTR $= 1.45$ and nozzle pressure ratio NPR $= 3.67$, is extended from the inlet through the nozzle exit and to the domain boundary, with the rest of the domain set to the reference far-field conditions.

4.4.2 Modal analysis

To construct and solve the eigenvalue problem (6), the RANS base-flow was linearly interpolated onto three meshes of sizes $(Nz, Nr) = \{(135, 387), (294, 387), (456, 552)\}$, that are stitched together using overkit (an

Table 4: Simulation parameters for the axisymmetric straight nozzle jet.

Domain size	$(L_z, L_r) = (91R, 50R)$
Grid points	$(N_z, N_r) = (721, 141)$
Nozzle length	$L_{nozzle}/R = 20$
Nozzle thickness	$t_{nozzle}/R = 0.0$
Reynolds number	$Re = \rho_j\ U_j R/\mu_j = 10^6$
Mach number	$U_j/c_j = 1.5$
TTR	$T_{0,inlet}/T_\infty = 1.45$
NPR	$p_{0,inlet}/p_\infty = 3.67$

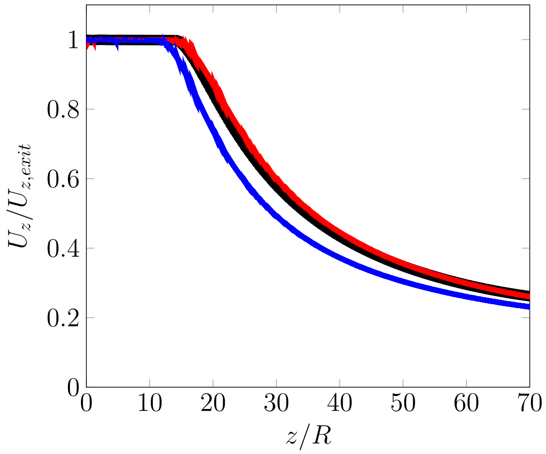

Figure 22: Non-dimensional centerline axial velocity corresponding to the RANS base-flow described in 4.4.1. The literature data from Jeun et al. (2016) is represented by ▬, the data from an OpenFOAM-8 RANS simulation without the turbulence model modifications is represented by ▬ and the data from an OpenFOAM-8 RANS simulation with the turbulence model modifications is represented by ▬.

Table 5: Thermo-physical and k-ϵ turbulence model parameters for the straight nozzle jet.

Sutherland model $(A_s,\, T_s)$	$(1.458 \times 10^{-6}, 110.4)$
C_μ	0.0874
C_1	1.4
C_2	2.02
C_3	0
σ_k	0.324
σ_ϵ	0.377
Pr_T	0.422

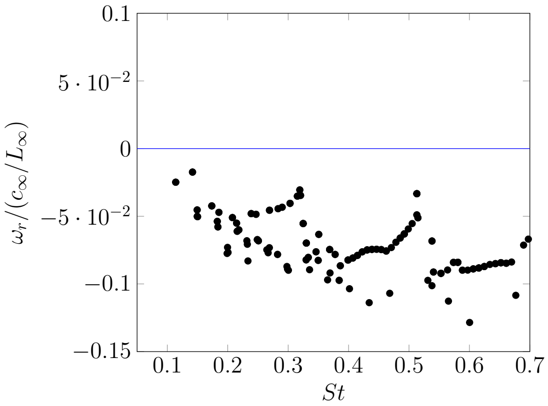

Figure 23: Stable eigenspectrum for the straight nozzle Mach 1.5 axisymmetric jet.

overset meshing tool). Our in-house code `PlasCom2` is then used to construct the linearized compressible Navier-Stokes operator. A similar interpolation procedure has been employed in (Natarajan, 2017) and mesh insensitivity to the quantities of interest was ensured. Fig. 23 shows the stable eigenspectrum of corresponding to the RANS base-flow $\bar{\boldsymbol{Q}}$, described in the previous section. Target eigenvalues $(\omega_{r,\text{target}}/(c_\infty/L_\infty), St_{\text{target}})$ were used with $\omega_{r,\text{target}}/(c_\infty/L_\infty) = 0.0$ and St target in the range of 0.05–0.65, with a spacing of $St_{\text{target}} = 0.05$. For each target eigenvalue, 5 eigenmodes were obtained using the convergence criterion $||\boldsymbol{L}\hat{\boldsymbol{Q}} - i\omega\hat{\boldsymbol{Q}}||/||i\omega\hat{\boldsymbol{Q}}|| \approx 10^{-8}$.

4.4.3 Non-modal analysis verification

In this section the input and output response of the linearized operator $\boldsymbol{L}$ is investigated at a Strouhal number $St = 0.33$. This analysis will require a singular value decomposition (SVD) of the operator $\boldsymbol{K} = \boldsymbol{N_r}\ \boldsymbol{H(\omega)}\ \boldsymbol{N_f^{-1}}$, as per the discussion in section 4.2. The expressions used to evaluate the left and right singular vectors, as part of the SVD, are as shown below

$$\boldsymbol{K}\ \boldsymbol{K}^H\ \hat{\boldsymbol{u}}_i = \sigma_i^2 \hat{\boldsymbol{u}}_i, \tag{19}$$

$$\boldsymbol{K}^H\ \boldsymbol{K}\ \hat{\boldsymbol{v}}_i = \sigma_i^2 \hat{\boldsymbol{v}}_i. \tag{20}$$

From the Eq. (9) it is clear that a matrix inversion is a part of this calculation. Additionally, the matrices $\boldsymbol{B}$ and $\boldsymbol{C}$ can be singular. Hence, to avoid the matrix inversion, the left ($\boldsymbol{U}$) and right ($\boldsymbol{V}$) singular vectors are computed using a user-defined matrix-vector-product, that utilizes a linear solve to evaluate terms such as $\boldsymbol{K}\hat{\boldsymbol{v}}_i$, in the above equations. The original expressions (from section 4.2) for gain, input and output modes of the system are then computed to yield a resolvent analysis of the linearized operator $\boldsymbol{L}$ given a Strouhal number. The results of the analysis for a $St = 0.33$, to compare with results from Jeun et al. (2016), are presented in Figs. 24 through 27.

Furthermore, Figs. 24 through 27 also indicate, through the regions highlighted by the boxed regions, the manner in which the matrices $\boldsymbol{B}$ and $\boldsymbol{C}$ select the inputs and outputs relevant to the current resolvent analysis. In the present study, we have chosen $\boldsymbol{B}$ to force the velocity in the immediate vicinity of the jet ($-10 < x/R < 60$ and $0.29 < r/R < 2.90$) and $\boldsymbol{C}$ to select far-field pressure ($-10 < x/R < 60$ and $8.70 < r/R < 39.2$). The spatial separation of input and output domains is motivated in part by the acoustic analogy approach (Goldstein, 2003) where acoustic sources are separated from acoustic propagation through an exact rearrangement of the compressible Navier-Stokes equations. In this view, acoustic sources are associated with unsteady turbulent flow and thus are restricted in space to the immediate vicinity of the jet. The effects, however, occur far away from the jet where acoustic propagation is important, but acoustic sources are inactive.

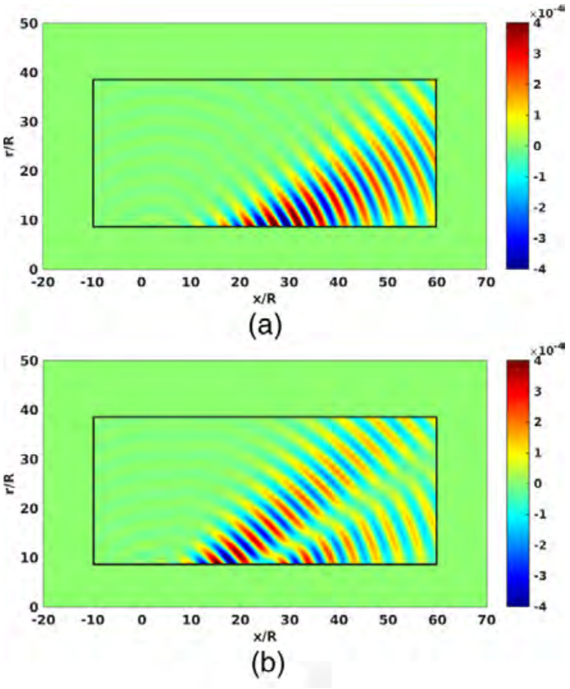

Figure 24: Optimal and first sub-optimal pressure response modes from Jeun et al. (2016), corresponding to the base flow described in 4.4.1. The boxed region and the pressure field are selected by the operator $\boldsymbol{C}$ (both in Jeun et al. (2016) and PlasCom2).

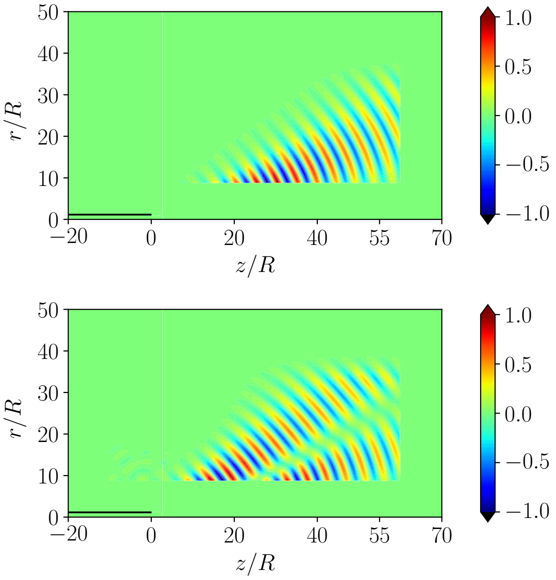

Figure 25: Optimal (top) and first sub-optimal (bottom) pressure response modes from `PlasCom2`, corresponding to the base flow described in 4.4.1.

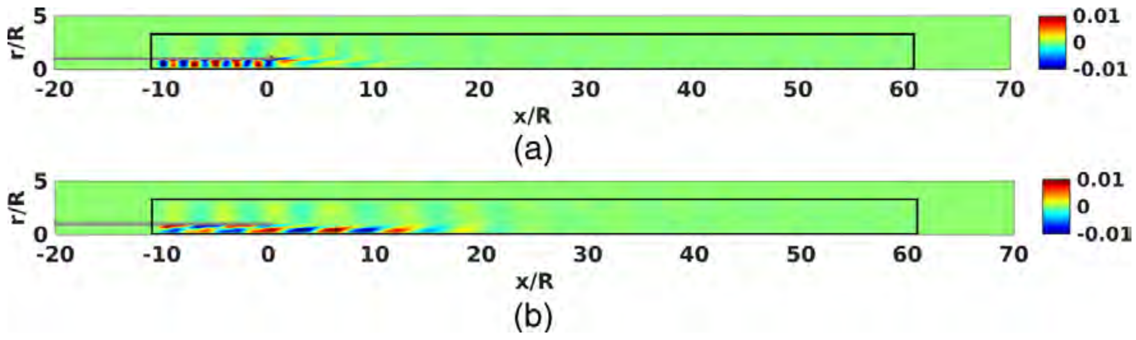

Figure 26: Optimal and first sub-optimal axial velocity forcing modes from Jeun et al. (2016), corresponding to the base flow described in 4.4.1. The boxed region and the axial velocity field are selected by the operator $\boldsymbol{B}$ (both in Jeun et al. (2016) and `PlasCom2`).

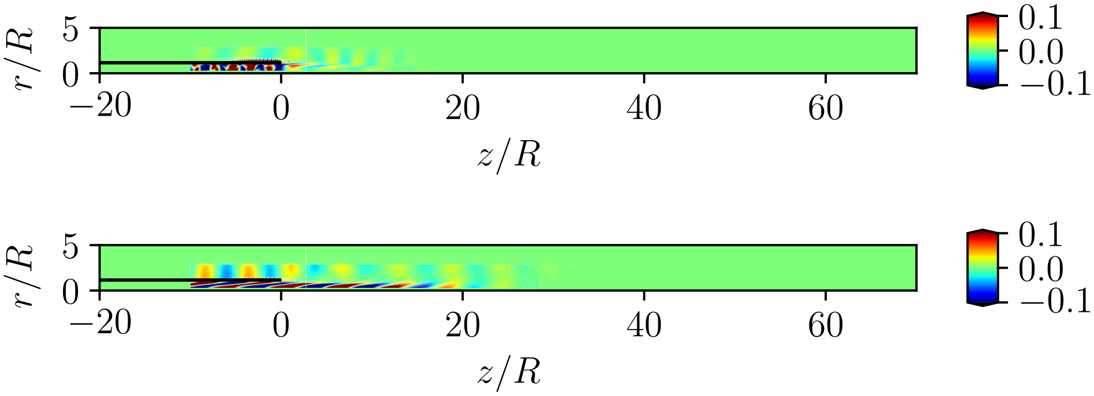

Figure 27: Optimal (top) and first sub-optimal (bottom) axial velocity forcing modes from `PlasCom2`, corresponding to the base flow described in 4.4.1.

4.4.4 FWH augmented non-modal analysis

In this section the input and output response of the linearized compressible Navier-Stokes operator $\boldsymbol{L}$, augmented with the FWH surface method, is again investigated at a Strouhal number $St = 0.33$. The manner in which the operator $\boldsymbol{F}$ extrapolates near-field information to the far-field is demonstrated in figure 28. Specifically, this figure shows how the linearized FWH surface method uses the convected Green's function ($\hat{G}_c$) to extrapolate the acoustic pressure field at a distance of $30R$ from the centerline axis of the jet, given the near-field acoustic pressure over the FWH surface located at $18R$.

4.5 Resolvent analysis based JNR on subsonic shock-free axisymmetric jets

In this section the application of resolvent based control, as a proof of concept, to an axisymmetric simulation of a subsonic jet issuing from a straight nozzle is described.

4.5.1 Flow solution

The simulation parameters are summarized in table 6. Three curvilinear computational grids of sizes $(Nz, Nr) = \{(135, 387), (294, 387), (456, 552)\}$, that are stitched together using overkit (an overset meshing tool within `PlasCom2`), are used to compute an axisymmetric simulation of subsonic jet flow through a straight nozzle (with radius R). The axisymmetric solver, within `PlasCom2`, computes the time-series data representing the evolution of flow-solution. This time-series data is then time-averaged to obtain $\bar{\boldsymbol{Q}}$, as shown in figure 29. An initial flow solution, corresponding to an inlet Mach number of 0.8, total temperature ratio (TTR) = 1.128 and nozzle pressure ratio (NPR) = 1.52434, is extended from the inlet through the nozzle exit and to the domain boundary, with the rest of the domain set to the reference far-field conditions. The nozzle wall boundary condition is modelled as an adiabatic slip wall (similar to Liu and Corrigan (2018)).

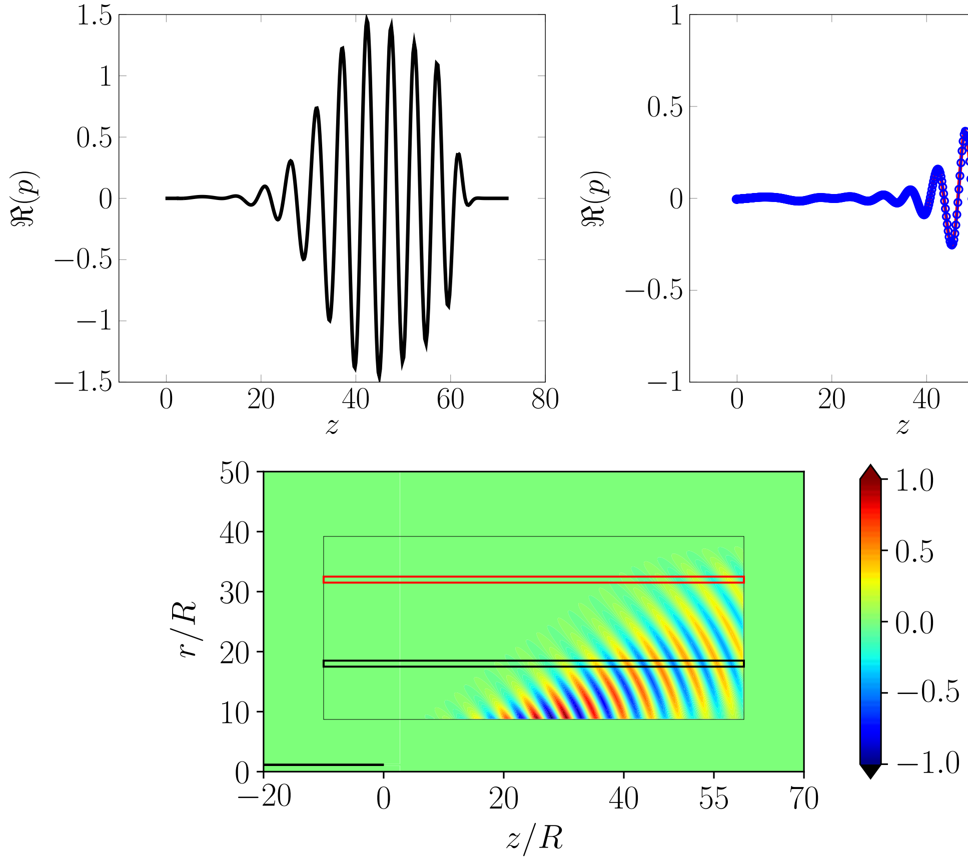

Figure 28: Verification of the linearized FWH far-field sound prediction operator $\boldsymbol{F}$ (described in section 4.2) acting on the output of $\boldsymbol{CQ'}$. The thin black and red rectangles over the resolvent response pressure field (bottom image) indicate the region over which the black (top left image) and red (top right image) curves of pressure data have been sampled. The blue curve in the top right plot indicates the FHW based prediction as per equation (13).

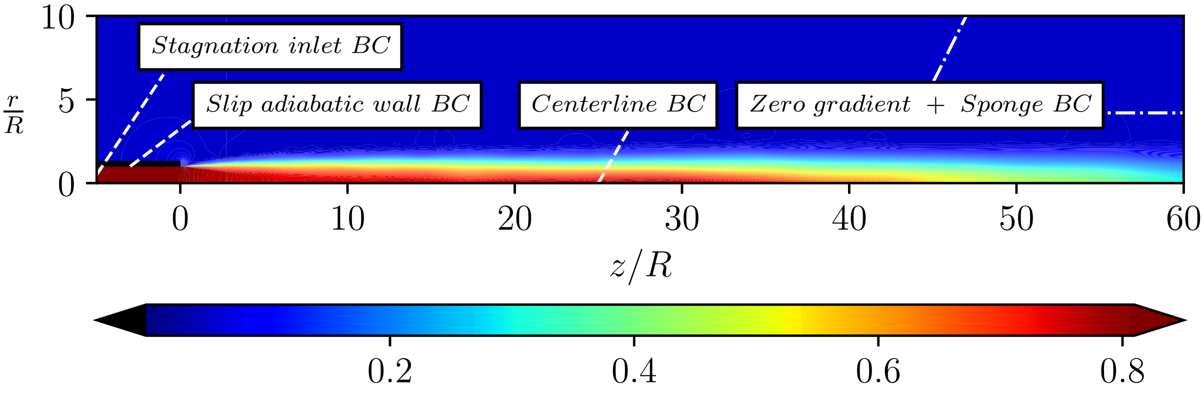

Figure 29: TTR = 1.13, NPR = 1.52, `plascom2x` laminar simulation of a straight nozzle subsonic flow time-averaged mach number contour plot.

Table 6: Axisymmetric simulation parameters for the subsonic flow through a straight nozzle jet.

Domain size	$(L_z, L_r) = (91R, 50R)$
Grid points mesh 1	$(N_{z,1}, N_{r,1}) = (135, 387)$
Grid points mesh 2	$(N_{z,2}, N_{r,2}) = (294, 387)$
Grid points mesh 3	$(N_{z,3}, N_{r,3}) = (456, 552)$
Nozzle length	$L_{nozzle}/R = 20$
Nozzle thickness	$t_{nozzle}/R = 0.3$
Reynolds number	$Re = \rho_j\ U_j R/\mu_j = 10^6$
Mach number	$U_j/c_j = 0.8$
TTR	$T_{0,inlet}/T_\infty = 1.128$
NPR	$p_{0,inlet}/p_\infty = 1.52434$

4.5.2 Resolvent analysis

The resolvent analysis procedure, described in sections 4.2 and 4.4.3, is used here to compute the optimal and sub-optimal gains/modes corresponding to the time-averaged base flow $\bar{\boldsymbol{Q}}$. Figure 30 shows the variation in optimal and sub-optimal gain as a function of Strouhal number. Figure 31 reveal the structure of the three largest optimal gain resolvent modes, and the manner in which they vary with Strouhal number. The optimal modes corresponding to both $St = 0.32$ and $St = 0.55$, feature beams of sound energy directed towards the acoustic region of the jet flow. Thus, identifying them as resolvent modes suitable for a structural sensitivity based gain reduction, since, suppressing the efficiency with which these modes radiate acoustic energy away from the hyrdrodynamic region and into the acoustic region of the jet flow, could be a path towards physics based JNR.

4.5.3 Structural sensitivity based control selection

In this section, JNR is demonstrated by using linear-feedback-control designed, using structural sensitivity analysis, to reduce the gain (σ) associated with the resolvent modes that are highly efficient at radiating sound energy towards the acoustic region of the jet flow. The procedure uses a wavemaker (Chomaz, 2005) like approach to determine which co-located state variables to sense/actuate and where they must be located. Specifically, for the flow described in section 4.5.1 and at the $St = 0.32$, as shown in the wavemaker like plots in figures 32 and 33, a ρV_z actuator with a co-located ρE sensor positioned close to the wall, at approximately $6R$ upstream of the nozzle exit, is able to modify the gain associated with the corresponding resolvent modes. This, however, is not the control capable of the largest change-in-gain ($d\sigma$) as per the resolvent based wavemaker plots. Yet it is chosen, since this choice of control offers the largest impact on resolvent gain whilst still in close proximity to the nozzle wall. A real actuator/sensor could be placed in

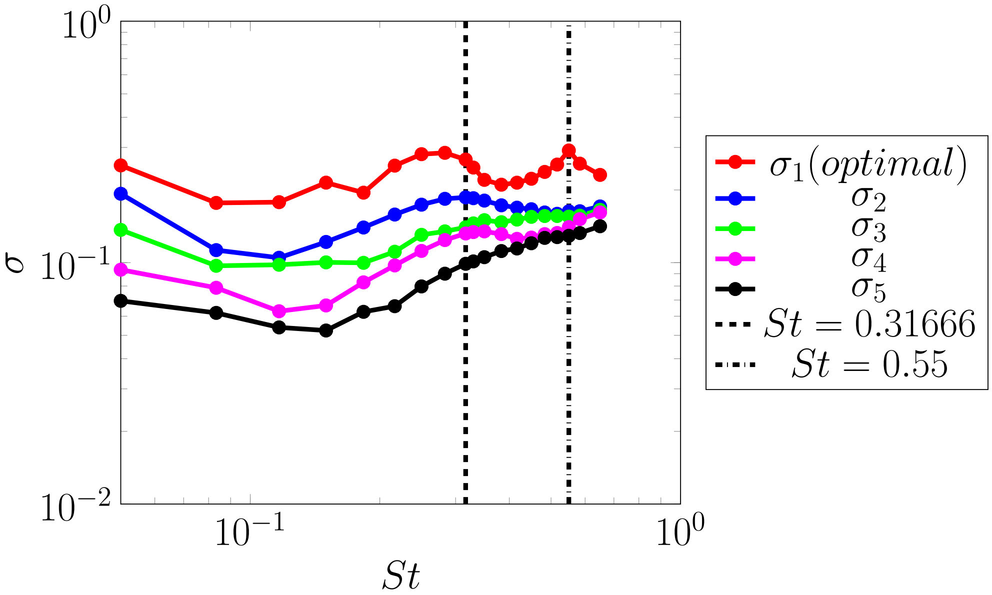

Figure 30: TTR = 1.128, NPR = 1.52434, optimal and sub-optimal resolvent gains corresponding to the `plascom2x` laminar simulation of a straight nozzle time-averaged subsonic flow.

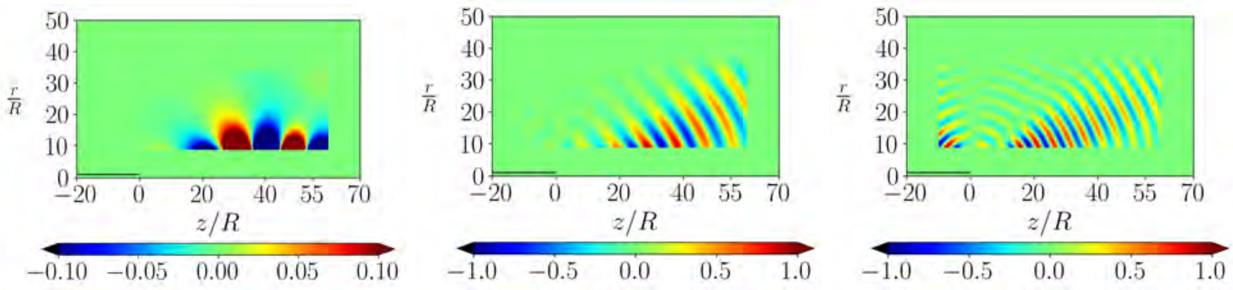

Figure 31: Optimal response mode (pressure field contour plot) corresponding to $St = 0.05$ (top left), $St = 0.31666$ (top right) and $St = 0.55$ (bottom) for the straight nozzle subsonic flow.

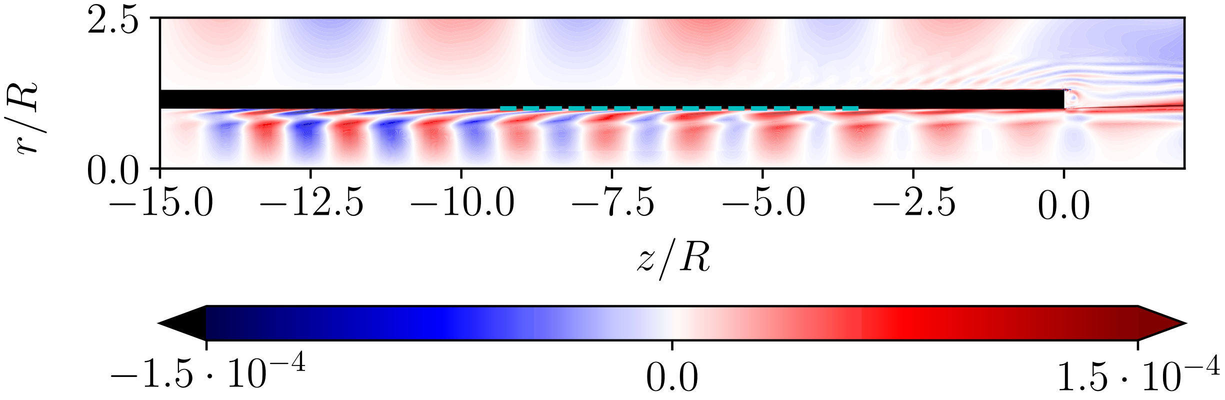

Figure 32: Wave-maker like regions ($Re\left(\hat{\boldsymbol{u}}^H(\boldsymbol{N}_r\boldsymbol{C}\ (\boldsymbol{R}\ \boldsymbol{dL}\ \boldsymbol{R})\ \boldsymbol{B}\boldsymbol{N}_f^{-1})\ \hat{\boldsymbol{v}}/(\hat{\boldsymbol{u}}^H\hat{\boldsymbol{u}})\right)$) corresponding to a ρV_z forcing and and ρE sensor collocated pair, at $St = 0.32$, for the straight nozzle subsonic flow. Additionally, the region where the linear-feedback-control is applied has been highlighted by a dashed cyan line.

such a location to achieve a similar JNR.

4.5.4 Jet noise reduction

This section showcases the effect of resolvent based linear-feedback-control on the jet noise produced by the flow described in section 4.5.1. To demonstrate this, acoustic pressure fluctuations from both the uncontrolled and controlled flows are measured and compared in terms of the overall and single frequency sound pressure level (SPL in dB). These measurements are sampled along a line l, located at $r/R = 20$ and $z/R \in [-8, 58]$ within the acoustic near-field region of the jet flow. The selection and placement of the actuator-sensor pair is computed using the resolvent modes corresponding to the frequency $St = 0.32$. This frequency was chosen on account of the low-polar-angle directivity of the beam of sound energy featured in the corresponding response mode (see figure 31), with the expectation that reducing the gain of this response mode would result in a reduction in pressure fluctuation amplitude over the region $z/R \in [40, 58]$ along line l.

The results of this resolvent based control on the jet flow, are demonstrated in figure 35, which shows a 2.5 dB reduction in overall sound pressure level along line l between $z/R \in [40, 55]$. Also, figure 36 shows a significant 2 to 6 dB reduction in sound pressure level at $St = 0.32$ (frequency corresponding to the resolvent modes used to inform the selection and placement of the control) along line l between $z/R \in [25, 58]$. Additionally, the contour plots in figures 37 show that there is a reduction in jet noise over $St \in [0.2, 0.4]$, whilst showing a simultaneous increase in SPL values close to $St = 0.55$. Figures 33 and 34 reveal the structure of the resolvent based wavemaker plots, close to the nozzle wall, corresponding to the frequencies $St = 0.32$ and $St = 0.55$. In case of $St = 0.31666$ as seen in figure 33 there is a net positive value associated with the wavemaker region close to the wall, about $6R$ behind the nozzle exit; which also corresponds to the region where control is applied (represented by line ▬ in figures 33 and 34). However, in this same region

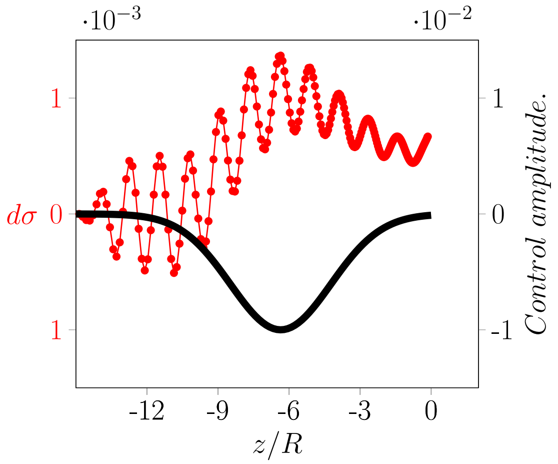

Figure 33: Line plot corresponding to the wave-maker like region $(Re\left(\hat{\boldsymbol{u}}^H(\boldsymbol{N}_r\boldsymbol{C}\ (\boldsymbol{R}\ \boldsymbol{dL}\ \boldsymbol{R})\ \boldsymbol{B}\boldsymbol{N}_f^{-1})\ \hat{\boldsymbol{v}}/(\hat{\boldsymbol{u}}^H\hat{\boldsymbol{u}})\right)$; represented by —●—) one grid point above the nozzle wall, at a $St = 0.32$, for the straight nozzle subsonic flow. Additionally, this figure also reveals the amplitude of the linear-feedback-control (represented by ▬) one grid point above the nozzle wall.

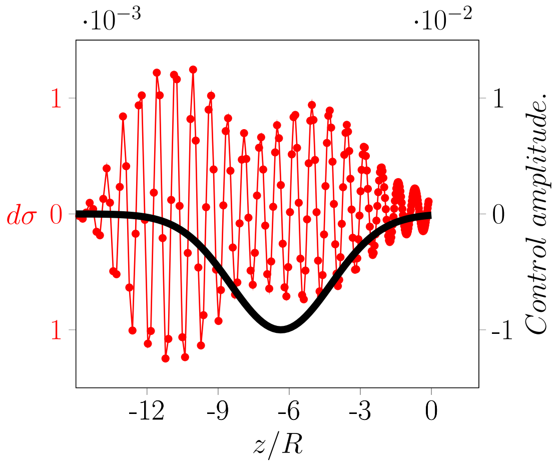

Figure 34: Line plot corresponding to the wave-maker like region $(Re\left(\hat{\boldsymbol{u}}^H(\boldsymbol{N}_r\boldsymbol{C}\ (\boldsymbol{R}\ \boldsymbol{dL}\ \boldsymbol{R})\ \boldsymbol{B}\boldsymbol{N}_f^{-1})\ \hat{\boldsymbol{v}}/(\hat{\boldsymbol{u}}^H\hat{\boldsymbol{u}})\right)$; represented by —●—) one grid point above the nozzle wall, at a $St = 0.55$, for the straight nozzle subsonic flow. Additionally, this figure also reveals the amplitude of the linear-feedback-control (represented by ▬) one grid point above the nozzle wall.

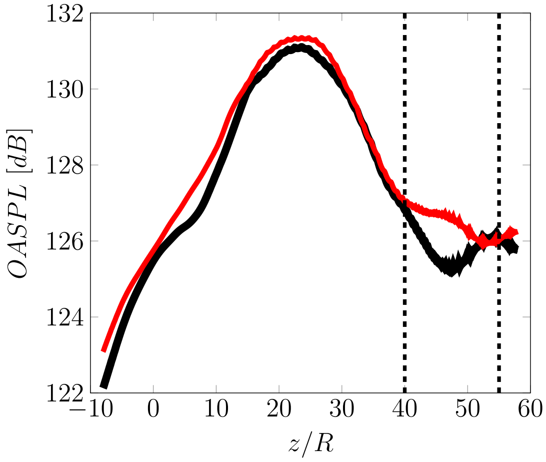

Figure 35: TTR = 1.13, NPR = 1.52, controlled (▬) and un-controlled (▬) OASPL plots from a `plascom2x` laminar simulation of a straight nozzle subsonic flow over the region defined by $r/R = 20$ and $z/R \in [-8, 58]$.

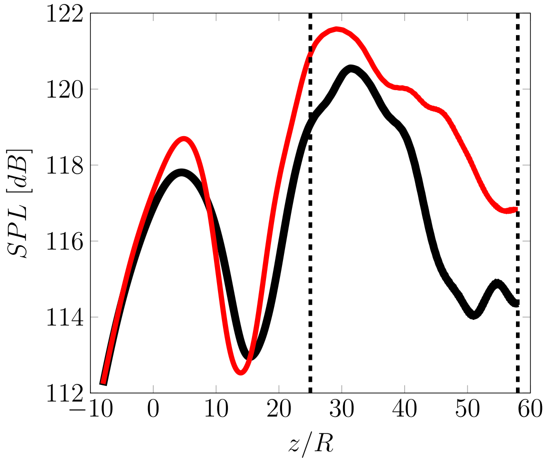

Figure 36: TTR = 1.13, NPR = 1.52, controlled (▬) and un-controlled (▬) SPL plots, corresponding to $St = 0.4$, from a `plascom2x` laminar simulation of a straight nozzle subsonic flow over the region defined by $r/R = 20$ and $z/R \in [-8, 58]$.

the resolvent based wavemaker plots corresponding to $St = 0.55$ have a predominately oscillatory nature, limiting the possibility of a cumulative reduction in gain on account of the control. Thus the applied base-flow modification is able to reduce noise at the lower Strouhal numbers, where the wavemaker structure is not predominately oscillatory, and is unable to reduce the noise at larger Strouhal numbers. Further analysis is necessary to ascertain a form of control that will not increase the acoustic oscillations at any frequency. However, the expected reduction in pressure fluctuation amplitude, over the region $z/R \in [40, 58]$ along line l, corresponding to $St = 0.31666$ is clearly demonstrated in figure 36.

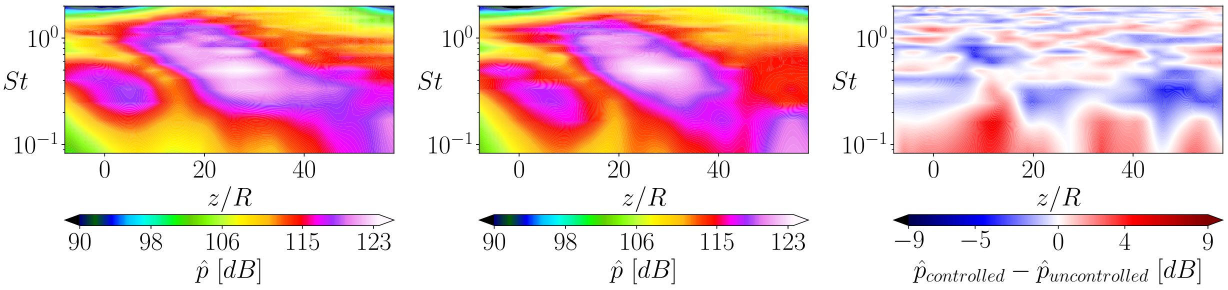

Figure 37: TTR = 1.13, NPR = 1.52, SPL contour plot corresponding to the un-controlled (left), controlled (center) and difference between the un-controlled and controlled (right) `plascom2x` laminar simulation of a straight nozzle subsonic flow over the region defined by $r/R = 20$ and $z/R \in [-8, 58]$.

4.6 Resolvent analysis based JNR on supersonic shock-laden axisymmetric biconical jets

An isolated and underexpanded jet, issuing from the biconical nozzle, is simulated using the same modified version of OpenFOAM-8, from section 4.4.1, to obtain a RANS mean-flow solution that can be used to study the jet's linear stability and non-modal response. Finally, the non-modal response is used to compute the location and extent of an optimal feedback controller, as described in section 4.3, to minimize the system's non-modal amplification at a given Strouhal number.

4.6.1 Flow solution

The simulation parameters are summarized in Tables 7 and 8. The stretched and curvilinear computational grid used has $(N_z, N_r) = (1331, 801)$ points in the axial and radial directions, respectively. A modified version of OpenFOAM-8, capable of incorporating the correct axisymmetric flow corrections to a RANS simulation using the standard k-ϵ model, provides a mean-flow solution $\bar{\boldsymbol{Q}}$. For the RANS calculation, an initial flow solution, corresponding to an inlet Mach number of 0.5, TTR = 3.0 and NPR = 4, is extended from the inlet through the nozzle exit and to the domain boundary, with the rest of the domain set to the reference far-field conditions.

Data from this RANS calculation is presented in Figs. 38a and 38b. This figure shows the contours of the RANS mean-flow Mach number and, a line plot of its centerline axial velocity (this plot includes a verification against data from Liu et al. (2013)).

Table 7: Simulation parameters for the axisymmetric biconical nozzle jet.

Domain size	$(L_z, L_r) = (35D_e, 25D_e)$
Grid points	$(N_z, N_r) = (1331, 801)$
Nozzle geometry details	See Fig. 1
Reynolds number	$\rho_\infty\, c_\infty R/\mu_\infty = 7.747 \times 10^5$
Nozzle exit Mach number	1.5
Total Temperature Ratio (TTR)	$T_{o,in}/T_\infty = 3.0$
Nozzle Pressure Ratio (NPR)	$p_{o,in}/p_\infty = 4.0$
Prandtl number (Pr)	0.71
γ	1.4

4.6.2 Global mode analysis

To construct and solve the eigenvalue problems (Eqs. (6)), the RANS base-flow was linearly interpolated onto three meshes of sizes $(Nz, Nr) = \{(102, 720), (139, 260), (306, 248)\}$, that are stitched together using overkit (an overset meshing tool). Our in-house code `PlasCom2` is then used to construct the linearized compressible

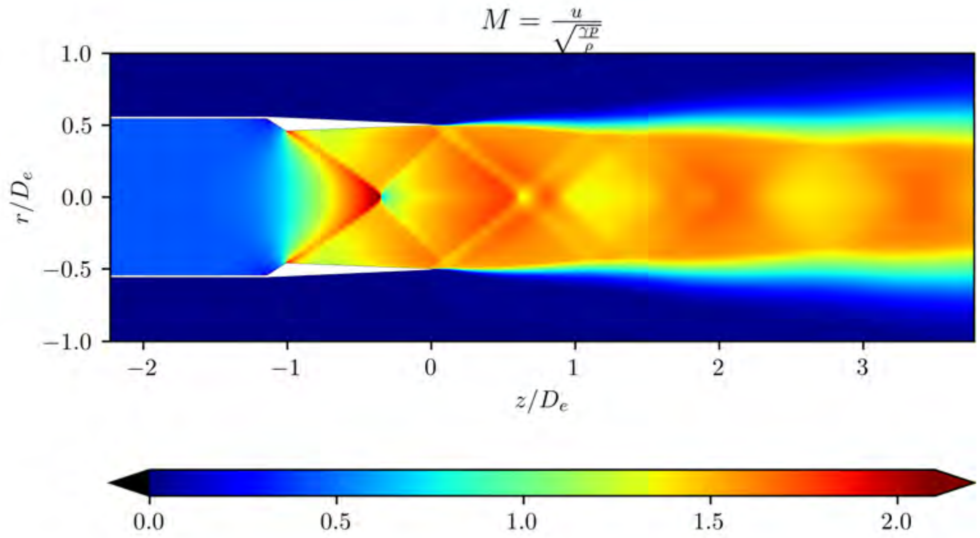

(a) Mach number contours.

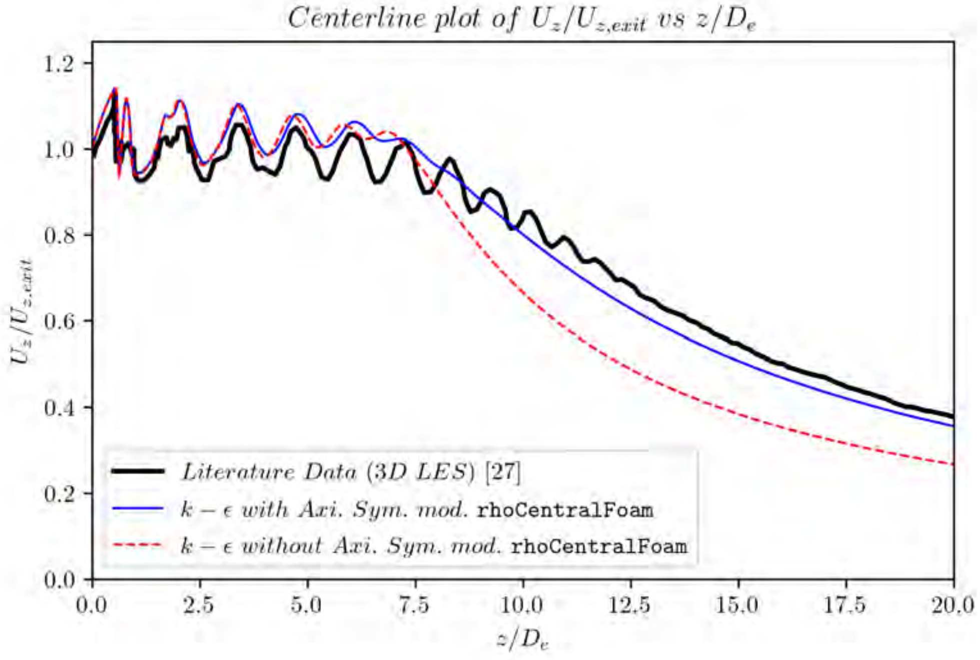

(b) Non-dimensional axial velocity profile at the centerline.

Figure 38: RANS base-flow of the axisymmetric biconical nozzle jet flow.

Table 8: Thermo-physical and k-ϵ turbulence model parameters for the axisymmetric biconical nozzle jet.

R	287.05 $[m^2 s^{-2} K^{-1}]$
C_p	1004.675 $[m^2 s^{-2} K^{-1}]$
Sutherland model (A_s, T_s)	$(1.458 \times 10^{-6}, 110.4)$
C_μ	0.0874
C_1	1.4
C_2	2.02
C_3	0
σ_k	0.324
σ_ϵ	0.377
Pr_T	0.422

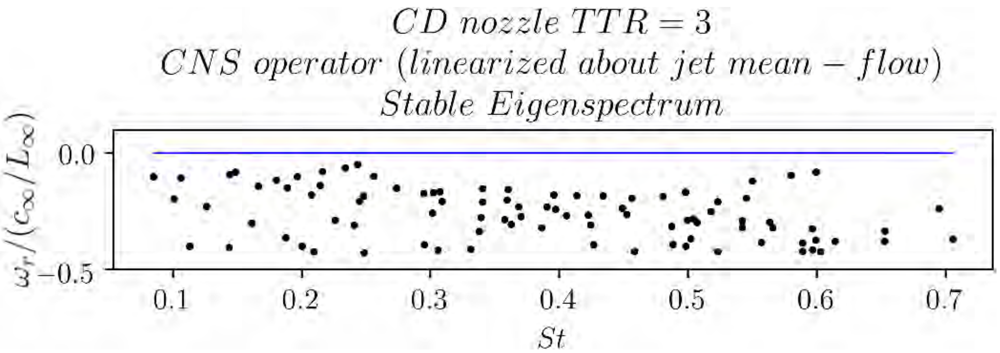

Figure 39: Eigenspectrum for the biconical nozzle axisymmetric jet, with exit Mach number 1.5, inlet TTR = 3 and inlet NPR = 4.

Navier-Stokes operator. A similar interpolation procedure has been employed in Natarajan (2017) ensuring mesh insensitivity to our quantities of interest. Target eigenvalues $(\omega_{r,\text{target}}/(c_\infty/L_\infty), St_{\text{target}})$ were used with $\omega_{r,\text{target}}/(c_\infty/L_\infty) = 0.0$ and St target in the range of 0.05–0.65, with a spacing of $St_{\text{target}} = 0.05$. For each target eigenvalue, 5 eigenmodes were obtained using the convergence criterion $||\boldsymbol{L}\hat{\boldsymbol{Q}} - i\omega\hat{\boldsymbol{Q}}||/||i\omega\hat{\boldsymbol{Q}}|| \approx 10^{-8}$. Fig. 39 shows the stable eigenspectrum of the RANS base-flow $\bar{\boldsymbol{Q}}$.

4.6.3 Resolvent analysis and structural-sensitivity based sensor-actuator placement

In this section the input and output responses of the LCNS operator, computed about the flow solution described in section 4.6.1, are investigated at three Strouhal numbers $St = \{0.3, 0.5, 0.7\}$, using the MATLAB software package as detailed in section 4.2 (Fig. 41 shows the gain associated with the optimal response mode as a function of St). These modes are then subject to the same structural sensitivity analysis based LCNS operator perturbation, verified in Murthy and Bodony (2022). The resulting sensor-actuator placement, in accordance with the control/forcing applied as per Eq. (15), is shown in Fig. 42 (actuator:ρ and sensor: ρE

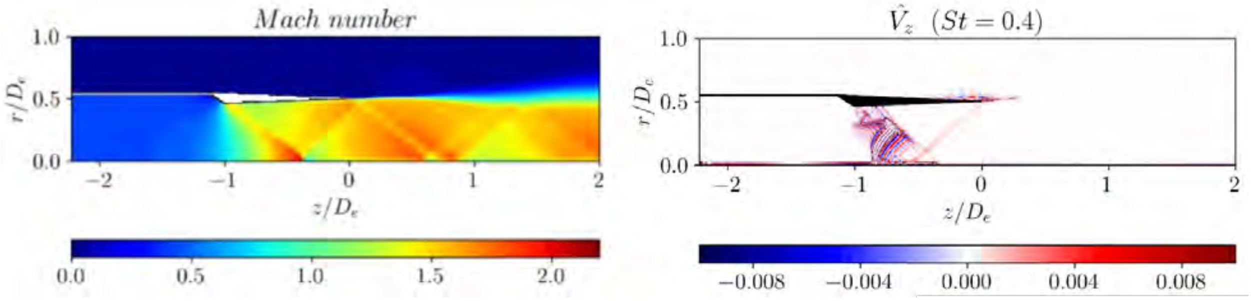

Figure 40: Visualization of the $m = 0$ forcing mode (right) corresponding to a standard resolvent analysis performed about LES mean-flow (left) data at $St = 0.4$ for the single biconical jet at TTR = 1 and NPR = 4.

was chosen as the change in gain was seen to be the highest with this pair).

4.7 Oddities in resolvent modes near strong shocks

Moving from the RANS based resolvent mode calculations to the LES based time-averaged mean-flows, as shown in figure 40, it was observed that within the biconical jet nozzle and close to the barrel shock, the resolvent modes seem to feature artifacts that questioned whether these resolvent modes were indeed faithfully connecting the near-field forcing to the far-field sound.

5 Convergent resolvent mode calculations in shock-laden flows

This section begins with the requirements for the construction of a physically-meaningful adjoint operator derived from the spatially-discretized non-linear operator were investigated by Bodony and Fikl (2022) using the inviscid Burgers' equation. The sections that follow attempt to use the converging numerical procedures identified in Bodony and Fikl (2022) to compute converging resolvent mode solutions.

The partial differential equations being discretized are non-linear, hence, artificial dissipation was used to regularize the solution when shocks formed. The general form of the first derivative operator used in the discretization was given by $\boldsymbol{D}_1[\vec{U}] = \boldsymbol{P}^{-1}\boldsymbol{Q}[\vec{U}]$ (with $\vec{U}$ is the base flow state). Additionally, the artificial dissipation was expressed in the following form $\boldsymbol{A}_D = -\boldsymbol{P}^{-1}\tilde{\boldsymbol{D}}_p^T\boldsymbol{\phi}[\vec{U}]\tilde{\boldsymbol{D}}_p$, where $\tilde{\boldsymbol{D}}_p$ is a finite difference approximation of the unscaled pth derivative. Using these operators, the following conditions on the derivative operator $\boldsymbol{Q}[\vec{U}]$ and the artificial dissipation term $\boldsymbol{\phi}[\vec{U}]$ were derived that ensured that adjoint solutions of the inviscid Burgers' equation would converge: (1) $\boldsymbol{\phi}[\vec{U}] > 0$, (2) $\boldsymbol{\phi}[\vec{U}]$ is differentiable with respect to $\vec{U}$, and (3) $\boldsymbol{Q}[\vec{U}]$ is differentiable with respect to $\vec{U}$. Though the three conditions are common sense, the work in Bodony and Fikl (2022) showed that neither the MUSCL (Leveque, 2002) scheme with flux limiters nor WENO schemes (Jiang and Shu, 1996) satisfy these requirements. Consequently, the use of MUSCL and WENO schemes, including all WENO variants, is not recommended for linearized analysis.

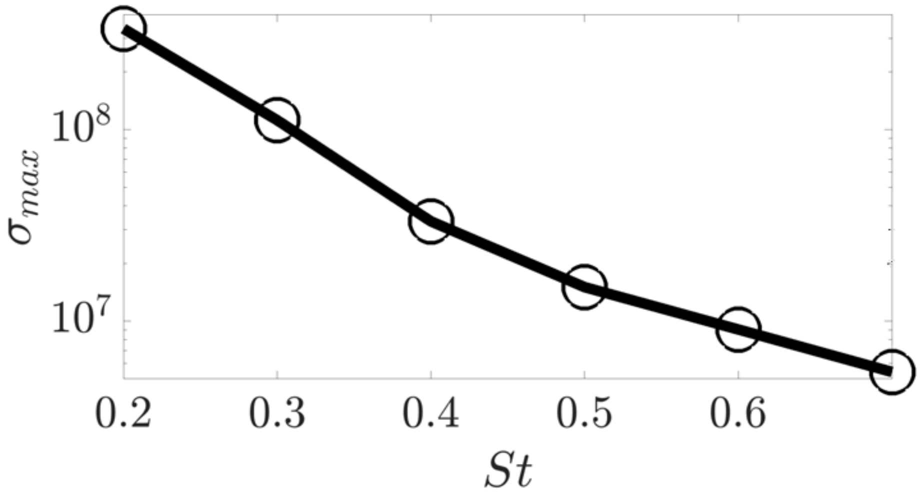

Figure 41: Optimal gain associated with the LCNS operator, computed using an OpenFOAM based RANS solution of an axisymmetric jet, through a biconical nozzle with exit Mach number 1.5, inlet TTR = 3 and inlet NPR = 4.

Local artificial diffusivity (LAD) schemes (e.g., the Jameson-Schmidt-Turkey (JST, Jameson et al. (1981)) scheme or more recent high-order versions (Kawai and Lele, 2008)) do satisfy every condition and were found in Bodony and Fikl (2022) to provide convergent adjoint solutions to the non-linear inviscid Burger's equation.

5.1 Derivation of semi-analytical resolvent modes in shock-laden flows

In this section, the work from Giles and Pierce (2001) and Giles et al. (1997) are used to investigate a convergent resolvent mode computation procedure using the Green's function operator corresponding to the forward and adjoint problems as described in Giles and Pierce (2001). This work is meant to extend the work of Bodony and Fikl (2022) to equations more relevant to CFD and to provide a semi-analytical resolvent calculation for verifying whether numerical methods give rise to meaningful linearized operators when shocks or other discontinuities are present. To the authors' knowledge, no comparable analysis exists. Due to the complexity of the analysis, only results from the quasi-one-dimensional equations are presently available.

5.1.1 Inviscid quasi-one-dimensional equations

The inviscid quasi-one-dimensional (quasi-1d) equations representing the compressible flow through a converging-diverging nozzle are given as

$$\vec{R}(\vec{U}, h) = \frac{d}{dx}\left(\vec{F}h\right) - \frac{dh}{dx}\vec{P}, \tag{21}$$

where,

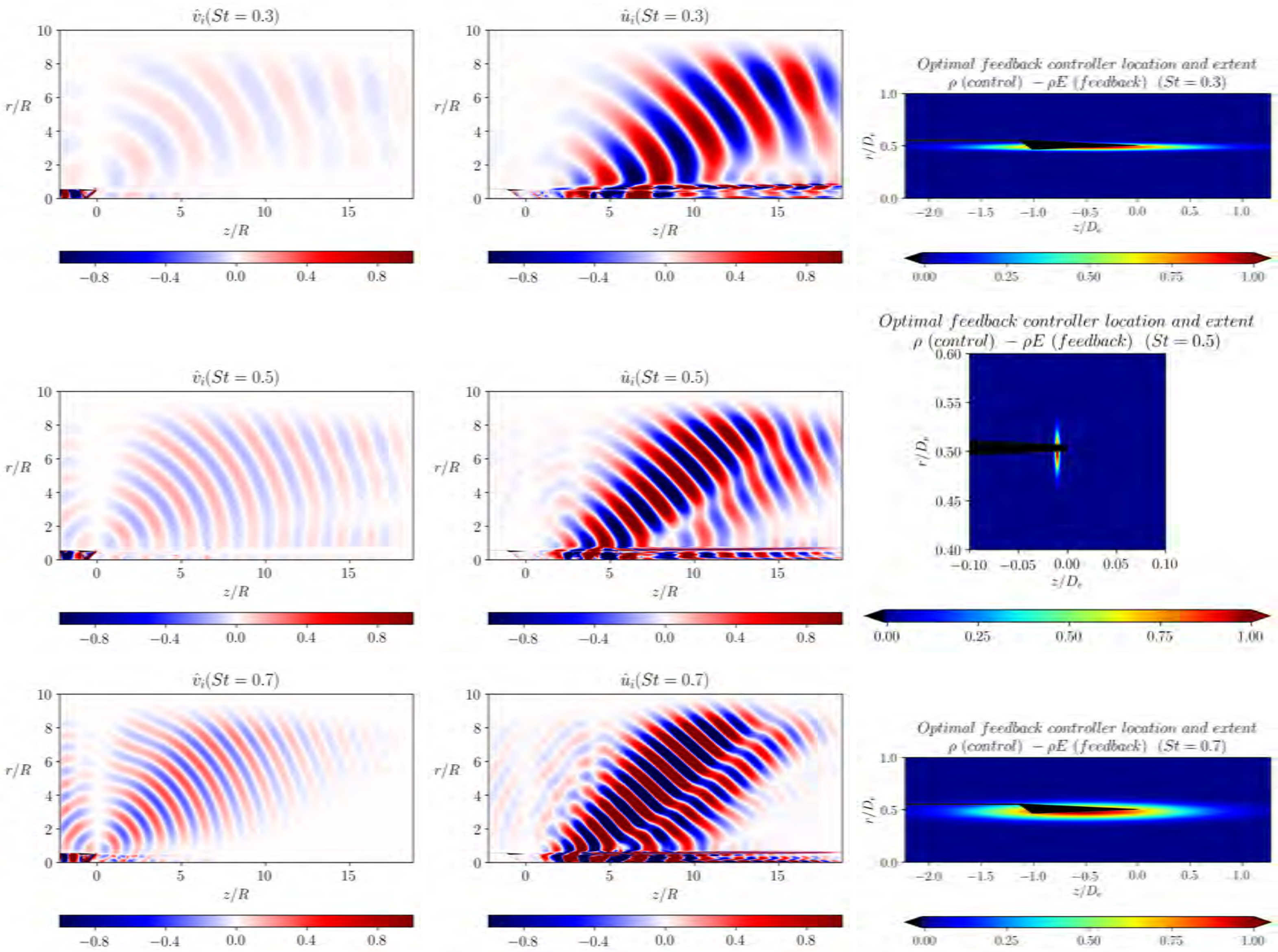

Figure 42: Resolvent analysis and structural-sensitivity based sensor-actuator placement as a function of St. Figures are arranged as input-modes, output-modes and the predicted sensor-actuator placement from left to right, additionally, they vary in Strouhal number from top to bottom.

$$\vec{U} = \begin{bmatrix} \rho \\ \rho q \\ \rho E \end{bmatrix}, \quad \vec{F} = \begin{bmatrix} \rho q \\ \rho q^2 + p \\ \rho q H \end{bmatrix}, \quad \vec{P} = \begin{bmatrix} 0 \\ p \\ 0 \end{bmatrix}, \tag{22}$$

and $H = E + \frac{p}{\rho} = \frac{\gamma}{\gamma - 1}\frac{p}{\rho} + \frac{1}{2}q^2$. Additionally, if the solution to the quasi-1d equations contains a discontinuity (at $x = x_s$) then the Rankine-Hugoniot jump conditions are given by

$$\left[\vec{F}\right]_{x_s^-}^{x_s^+} = 0. \tag{23}$$

5.1.2 Forward Green's function

The Green's function operator $\boldsymbol{G}(x, \xi)$ of the forward linearized problem is derived, exactly as presented in Giles and Pierce (2001), by first constructing three homogeneous solutions to the linear problem $\boldsymbol{L}\vec{u}_i = 0$, where $\boldsymbol{L}\vec{u}_i = d(h(x)\ \boldsymbol{A}(x)\ \vec{u}_i)/dx - dh/dx\ \boldsymbol{B}(x)\ \vec{u}_i$, $\boldsymbol{A}(x) = d\vec{F}/d\vec{U}$, $\boldsymbol{B}(x) = d\vec{P}/d\vec{U}$ and $\vec{P} = [0, p, 0]^T$. Next, a solution to an impulse-type-forcing of the form $\vec{f}_i(\xi)\ \delta(x - \xi)$ is constructed as a piece-wise solution of two homogeneous solutions $a_{1,i}\vec{u}_i + a_{2,i}\vec{u}_i$ (with summation over repeated indices and $\delta(x)$ the Dirac delta distribution), one before and the other after the location where the impulse type forcing is applied. The vector $\vec{f}_i$ is then computed by integrating the equation representing the linear problem across the location where the impulse-type-forcing is applied $\int_{\xi^-}^{\xi^+} \boldsymbol{L}\vec{u}_i(x, \xi)\ dx = \vec{f}_i(\xi)$. Then, the Green's function operator is constructed using the vectors $\vec{u}_i(x, \xi)$ and $\vec{f}_i(\xi)$ as shown below

$$\boldsymbol{G}(x, \xi) = (\vec{u}_1(x, \xi) \mid \vec{u}_2(x, \xi) \mid \vec{u}_3(x, \xi)) \left(\vec{f}_1(\xi) \mid \vec{f}_2(\xi) \mid \vec{f}_3(\xi)\right)^{-1}, \tag{24}$$

where vertical lines indicate the partitioning of the row vector and array into three columns.

5.1.3 Adjoint Green's function

Similar to the construction of the forward Green's function, the Green's function for the adjoint problem can be constructed using three linearly independent gradient functions ($\vec{g}_i$) and corresponding adjoint solutions ($\vec{v}_i$), such that $\boldsymbol{L}^\dagger \vec{v}_i(x, \eta) = \vec{g}_i(\eta)\delta(x - \eta)$. To accomplish this, three objective functions, $J_1(x) = \int_{-1}^{1} p(x)\ dx$, $J_2(x) = \int_{-1}^{1} T(x)\ dx$, $J_3(x) = \int_{-1}^{1} q(x)\ dx$ are defined. The corresponding gradients ($dp/d\vec{U}$, $dT/d\vec{U}$ and $dq/d\vec{U}$) of the objective function integrands (k_i such that $J_i = \int_{-1}^{1} k_i(x)\,\mathrm{d}x$) are then used to evaluate,

$$\begin{aligned} dJ_{i,j} = I_{i,j}(\xi, \eta) \quad &= \quad \int_D \Big\{ \vec{u}_j(x, \xi) \cdot \frac{\partial k_i(\eta)}{\partial \vec{U}} \delta(x - \eta) \\ &\quad - k_i(\eta)\ \delta(x - \eta)\ \delta(x - x_s^+)\ \delta_j(\xi) \\ &\quad + k_i(\eta)\ \delta(x - \eta)\ \delta(x - x_s^-)\ \delta_j(\xi) \Big\}\ dx \\ &= \quad \vec{u}_j(\eta, \xi) \cdot \vec{g}_i(\eta) \\ &\quad - k_i(\eta)\ \delta(\eta - x_s^+)\ \delta_j(\xi) \end{aligned} \tag{25}$$

$$+ k_i(\eta)\ \delta(\eta - x_s^-)\ \delta_j(\xi), \tag{26}$$

where δ_j represents the linearized displacement in the shock location and the indices i and j represent the choice of objective function and forcing (ρuh, H or p_0) used to compute the perturbation $I_{i,j}$, respectively. Then, the operator $(I_{i,1}(\xi,\eta) \mid I_{i,2}(\xi,\eta) \mid I_{i,3}(\xi,\eta))$ is used to evaluate

$$\vec{v}_i^T(\xi,\eta) = (I_{i,1}(\xi,\eta) \mid I_{i,2}(\xi,\eta) \mid I_{i,3}(\xi,\eta))\ \left(\vec{f}_1(\xi) \mid \vec{f}_2(\xi) \mid \vec{f}_3(\xi)\right)^{-1}, \tag{27}$$

which is used to obtain the Green's function for the adjoint problem, as shown in Eq. (24). Here, $\vec{u}_i(x,\xi)$ is replaced by $\vec{v}_i(x,\eta)$ and $\vec{f}_i(\xi)$ with $\vec{g}_i(\eta)$ to evaluate $\boldsymbol{G}_s^\dagger(x,\eta)$, as shown below

$$\boldsymbol{G}_s^\dagger(x,\eta) = (\vec{v}_1(x,\eta) \mid \vec{v}_2(x,\eta) \mid \vec{v}_3(x,\eta))\ (\vec{g}_1(\eta) \mid \vec{g}_2(\eta) \mid \vec{g}_3(\eta))^{-1}. \tag{28}$$

The adjoint solution corresponding to any given $\vec{g}(\eta)$ can then be computed as

$$\vec{v}(x) = \int_D \boldsymbol{G}^\dagger(x,\eta)\ \vec{g}(\eta) d\eta\ -\ \boldsymbol{\Phi}^{-T}(x) \begin{Bmatrix} \delta_1(x) \\ 0 \\ \delta_3(x) \end{Bmatrix} \left[(p \mid T \mid q)\ \boldsymbol{\Gamma}^{-1}\ \vec{g}\right]_{x_s^-}^{x_s^+}, \tag{29}$$

where $\boldsymbol{G}^\dagger(x,\eta) = \boldsymbol{\Phi}^{-T}(x) \begin{bmatrix} \vec{u}_1(\eta,x)^H \\ \vec{u}_2(\eta,x)^H \\ \vec{u}_3(\eta,x)^H \end{bmatrix}$, $\boldsymbol{\Phi}(x) = \left(\vec{f}_1(x) \mid \vec{f}_2(x) \mid \vec{f}_3(x)\right)$ and $\boldsymbol{\Gamma}(x) = (\vec{g}_1(x) \mid \vec{g}_2(x) \mid \vec{g}_3(x))$.

5.1.4 Procedure to construct the zero-frequency resolvent operator

The zero frequency resolvent modes (forcing modes $\hat{f}$ and response modes $\hat{r}$) are constructed by solving for the forcing $\hat{f}$, that will maximize the gain σ using the Green's function operators of the forward and adjoint problems, which were derived in the previous subsections, as follows

$$\sigma^2 = \max_{\hat{f}} \left(\frac{\langle \hat{r}, \hat{r} \rangle}{\left\langle \hat{f}, \hat{f} \right\rangle} \right) = \max_{\hat{f}} \left(\frac{\left\langle \boldsymbol{G} * \hat{f}\ ,\ \boldsymbol{G} * \hat{f} \right\rangle}{\left\langle \hat{f}\ ,\ \hat{f} \right\rangle} \right) = \max_{\hat{f}} \left(\frac{\left\langle \hat{f}\ ,\ \boldsymbol{G}^\dagger * \boldsymbol{G} * \hat{f} \right\rangle}{\left\langle \hat{f}\ ,\ \hat{f} \right\rangle} \right). \tag{30}$$

A normalized power iteration method is used to solve the eigenvalue problem $\boldsymbol{G}^\dagger * \boldsymbol{G} * \hat{f} = \sigma^2 \hat{f}$. This produces a solution to the most-amplified-forcing ($\hat{f}$) and most-receptive-response ($\hat{r}(x) = \int_D \boldsymbol{G}(x,\xi)\hat{f}(\xi)d\xi$) mode corresponding to the linear system $\boldsymbol{L}\hat{r} = \hat{f}$.

5.1.5 Zero-Frequency Resolvent Analysis of Shock-Laden Quasi-1d Flow

In this section, the zero-frequency resolvent modes corresponding to steady flow through a duct of cross-section $h(x)$ and governed by the quasi-one-dimensional Euler equations (21) are computed using the procedure described in section 5.1.4 and compared against the same modes computed using a finite volume method (FVM) fitted with the JST scheme as described in Murthy and Bodony (2022).

Inviscid flow solution

Two steady quasi-1d isentropic flows, one supersonic and the other subsonic, through a CD nozzle are considered. The geometric definition of the CD nozzle is given by

$$h(x) = \begin{cases} 2 & (-1 \leq x \leq -1/2) \\ 1 + \sin^2(\pi x) & (-1/2 < x < 1/2) \\ 2 & (1/2 \leq x \leq 1). \end{cases} \tag{31}$$

In case of the supersonic flow, the inlet is set to a non-dimensional (as per Giles and Pierce (2001)) stagnation enthalpy $H_{\text{in}} = 4$, stagnation pressure $p_{0,\text{in}} = 2$ and Mach number $M_{\text{in}} = 3$. And, in case of the subsonic flow the inlet is set to the same stagnation conditions, but a different exit condition where the static pressure $p_{ex} = 1.98$. Finally, a flow with the same inlet conditions and a different exit static pressure $p_{ex} = 1.6$ is considered. This exit boundary condition generates a steady quasi-1d flow that features a shock in the diverging section of the CD nozzle.

The isentropic flows are chosen to verify the derivation for the zero-frequency resolvent modes corresponding to the quasi-1d flow through a CD nozzle, given in section 5.1.4. The shock-laden case is selected to investigate a discrete numerical methodology (similar to Murthy and Bodony (2022)) that can converge to the verified zero-frequency resolvent mode solutions computed as per section 5.1.4.

Resolvent modes corresponding to inviscid shock free base-flows

The zero-frequency resolvent ($\boldsymbol{R}(\omega = 0)$) modes corresponding to the shock free isentropic flows are computed by solving the eigenvalue problem that originates when computing the SVD of the resolvent operator, given by

$$\boldsymbol{R}^H(\omega = 0)\ \boldsymbol{R}(\omega = 0)\ \vec{f} = \boldsymbol{G}^\dagger * \boldsymbol{G} * \vec{f} = \sigma^2 \vec{f}, \tag{32}$$

(here $*$ represents the convolution operation), and are in agreement, as shown in Figs. 43, 44, 45 and 46, with the results of the resolvent analysis procedure described in Murthy and Bodony (2022).

Resolvent modes corresponding to inviscid shock-laden base-flows

The first step towards a numerical procedure capable of producing convergent resolvent modes in shock-laden baseflows is to show that the numerical procedure and governing quasi-1d equations detailed in preceding sections, can produce converging adjoint modes corresponding to a quasi-1d shock-laden base-flow. Figs. 47 and 48 show that using a linear finite volume method, with a shock capturing mechanism that is a composite differentiable function of derivatives of the forward flow solution, it is possible to build a numerical procedure that can converge to the adjoint ($\vec{\nu}$) and forward solutions ($\vec{u}$; here convergence is only in a pointwise sense except at $x = x_s$), computed as per Giles and Pierce (2001), corresponding to a shock-laden base-flow, a specific gradient ($\vec{g}$) and forcing ($\vec{f}$; as defined in section 5.1.2) function, respectively.

However, resolvent operators constructed using the forward ($\boldsymbol{L}$) and adjoint ($\boldsymbol{L}^\dagger$) operators, used in the previous section to obtain Figs. 47 and 48, do not produce resolvent modes that converge to the resolvent modes computed using equation (30; as seen in Fig. 49). This suggests that the zero-frequency resolvent modes constructed using the equations

$$(\boldsymbol{L}^{-1})^{\dagger}\ \boldsymbol{L}^{-1}\ \vec{f} = \sigma^2 \vec{f} \quad \& \quad \vec{r} = \boldsymbol{L}^{-1}\ \vec{f} \tag{33}$$

are not equal to the modes computed using the equations

$$\boldsymbol{G}^{\dagger} * \boldsymbol{G} * \vec{f} = \sigma^2 \vec{f} \quad \& \quad \vec{r} = \boldsymbol{G} * \vec{f} \tag{34}$$

when the shock-laden base-flows are considered.

5.1.6 A viscous extension of Giles and Pierce (2001)

To better understand why resolvent modes corresponding to shock-laden flows do not agree with the numerical solutions, that feature inherent artificial viscosity, we consider two questions

1. Are the resolvent modes computed as per equations (34) physical? That is, in the limit of vanishing viscosity do modes computed as per a viscous extension of equations (34) approach the inviscid modes computed as per equations (34); and shown in ▬ on figure 49.
2. Do the modes computed using the numerical procedure, as per equations (33), converge to the physical analytical adjoint modes computed as per equations (34).

Viscous flow equations

To answer these questions the procedure to compute resolvent modes, as per (34), need to be extended to consider viscous quasi-1d flows as shown below

$$\vec{R}(\vec{U}, h) = \frac{d}{dx}(h\vec{F}) + \frac{d}{dx}\left(h\frac{d}{dx}(\vec{F}_{v,1})\right) + \frac{dh}{dx}\frac{d}{dx}(\vec{F}_{v,2}) - \frac{dh}{dx}\vec{P} = 0, \tag{35}$$

where

$$\vec{U} = \begin{bmatrix} \rho \\ \rho q \\ \rho E \end{bmatrix},\ \vec{F} = \begin{bmatrix} \rho q \\ \rho q^2 + p \\ \rho q H \end{bmatrix},\ \vec{F}_{v,1} = \begin{bmatrix} 0 \\ -\frac{4\mu q}{3} \\ -\frac{2\mu q^2}{3} - \frac{c_p \mu T}{Pr} \end{bmatrix},\ \vec{F}_{v,2} = \begin{bmatrix} 0 \\ \frac{4\mu q}{3} \\ 0 \end{bmatrix},\ \vec{P} = \begin{bmatrix} 0 \\ p \\ 0 \end{bmatrix}, \tag{36}$$

where, $H = E + \frac{p}{\rho} = \frac{\gamma}{\gamma - 1}\frac{p}{\rho} + \frac{1}{2}q^2$.

Viscous linear forward operator and basis solutions $\vec{u}_{j\in[1,2,3]}(x, \xi)$

Starting with these viscous quasi-1d non-linear equations, the corresponding viscous linear forward operator $\boldsymbol{L}_{viscous}$ can be computed starting with the perturbed non-linear equations as shown below

$$\vec{R} + \epsilon \boldsymbol{L}_{viscous}\vec{u}\ + \dots \ = \ \frac{d}{dx}(h(\vec{F} + \epsilon\ d\vec{F}\ + \dots)) + \frac{d}{dx}\left(h\frac{d}{dx}(\vec{F}_{v,1} + \epsilon\ d\vec{F}_{v,1}\ + \dots)\right) + \frac{dh}{dx}\frac{d}{dx}(\vec{F}_{v,2} + \epsilon\ d\vec{F}_{v,2}\ + \dots)$$

$$
\begin{aligned}
&\quad -\frac{dh}{dx}(\vec{P} + \epsilon \; d\vec{P} \;\; + \dots) \\
\Rightarrow \boldsymbol{L}_{viscous}\vec{u} \;\; &= \;\; \frac{d}{dx}\left(h \; \frac{\partial \vec{F}}{\partial \vec{U}} \; \vec{u}\right) + \frac{d}{dx}\left(h \frac{d}{dx}\left(\frac{\partial \vec{F}_{v,1}}{\partial \vec{U}} \; \vec{u}\right)\right) + \frac{dh}{dx}\frac{d}{dx}\left(\frac{\partial \vec{F}_{v,2}}{\partial \vec{U}} \; \vec{u}\right) - \frac{dh}{dx}\frac{\partial \vec{P}}{\partial \vec{U}} \; \vec{u}. \qquad (37)
\end{aligned}
$$

Using this viscous forward linear operator, and similar to Giles and Pierce (2001), homogeneous forward solutions ($\vec{u}(x,\xi)$) that satisfy the following equation

$$
\int_D \boldsymbol{L}_{viscous}\vec{u}_j(x,\xi)d\xi = \int_D \delta(x-\xi) \; \vec{f}_j(\xi)d\xi, \qquad (38)
$$

can be computed by considering solutions of the following form

$$
\begin{aligned}
\vec{u}(x,\xi) \;\; &= \;\; a \; H(x-\xi) \; \left(\frac{1}{h(x)}\frac{\partial \vec{U}}{\partial m}\bigg|_{H,q} + c_m(x,\xi) \; \frac{\partial \vec{U}}{\partial q}\bigg|_{m,H}\right) \\
&\quad + b \; H(x-\xi) \; \left(\frac{\partial \vec{U}}{\partial H}\bigg|_{m,q} + c_H(x,\xi) \; \frac{\partial \vec{U}}{\partial q}\bigg|_{m,H}\right) \\
&\quad + c \; H(-(x-\xi)) \; \left(\frac{1}{h(x)}\frac{\partial \vec{U}}{\partial m}\bigg|_{H,q} + c_q(x,\xi) \; \frac{\partial \vec{U}}{\partial q}\bigg|_{m,H}\right), \qquad (39)
\end{aligned}
$$

where, a and b represent uniform perturbations since the nonlinear quasi-1d equations ensure that mass flux and stagnation enthalpy (when $Pr = 3/4$) remain constant along the CD nozzle. The variable c is a uniform amplitude term and the functions $c_m(x,\xi), c_H(x,\xi)$ and $c_q(x,\xi)$ represent the non-uniform velocity field perturbations that ensure that $\boldsymbol{L}_{viscous}\vec{u}(x,\xi) = \vec{0}$, by satisfying the following homogeneity equations

$$
\begin{aligned}
\boldsymbol{L}_{viscous}\left\{a \; H(x-\xi) \; \left(\frac{1}{h(x)}\frac{\partial \vec{U}}{\partial m}\bigg|_{H,q} + c_m(x,\xi) \; \frac{\partial \vec{U}}{\partial q}\bigg|_{m,H}\right)\right\} = \boldsymbol{L}_{viscous}\vec{u}_1(x,\xi) \;\; &= \;\; \vec{0}, \\
\boldsymbol{L}_{viscous}\left\{b \; H(x-\xi) \; \left(\frac{\partial \vec{U}}{\partial H}\bigg|_{m,q} + c_H(x,\xi) \; \frac{\partial \vec{U}}{\partial q}\bigg|_{m,H}\right)\right\} = \boldsymbol{L}_{viscous}\vec{u}_2(x,\xi) \;\; &= \;\; \vec{0}, \\
\boldsymbol{L}_{viscous}\left\{c \; H(-(x-\xi)) \; \left(\frac{1}{h(x)}\frac{\partial \vec{U}}{\partial m}\bigg|_{H,q} + c_q(x,\xi) \; \frac{\partial \vec{U}}{\partial q}\bigg|_{m,H}\right)\right\} = \boldsymbol{L}_{viscous}\vec{u}_3(x,\xi) \;\; &= \;\; \vec{0}. \qquad (40)
\end{aligned}
$$

Viscous linear adjoint equations and operator

The adjoint equations and operator can be derived by considering the augmented nonlinear objective function (J), where the adjoint solution $\vec{v}$ enforces the differential flow constraints as shown below

$$
J = \int_D p \; dx - \int_D \vec{v}^T \cdot \vec{R} \; dx. \qquad (41)
$$

Linearizing this with respect to perturbations in the flow solution $\vec{u}$ with gradient $\vec{g}$, gives

$$
\begin{aligned}
dJ = I \;\; &= \;\; \int_D \vec{g}^T \cdot \vec{u} \; dx - \int_D \vec{v}^T \cdot \left(\; \boldsymbol{L}_{viscous} \; \vec{u} - \vec{f} \; \right) dx, \qquad (42) \\
\Rightarrow I \;\; &= \;\; \int_D \left(\frac{\partial p}{\partial \vec{U}}\right)^T \cdot \vec{u} \; dx - \int_D \vec{v}^T \cdot \left(\; \boldsymbol{L}_{viscous} \; \vec{u} - \vec{f} \; \right) dx, \qquad (43)
\end{aligned}
$$

$$\Rightarrow I \quad = \quad \int_D \vec{\nu}^T \cdot \vec{f} dx - \int_D \left\{ \vec{\nu}^T \cdot (\boldsymbol{L}_{viscous}\ \vec{u}) - \left(\frac{\partial p}{\partial \vec{U}} \right)^T \cdot \vec{u}\ \right\} dx. \tag{44}$$

Next the integration by parts procedure is used to transfer the differential operator $\boldsymbol{L}_{viscous}$ from $\vec{u}$ to the variable $\vec{\nu}$ as shown below and starting with

$$\begin{aligned} I \quad = \quad & \int_D \vec{\nu}^T \cdot \vec{f}\ dx \\ & - \int_D \vec{\nu}^T \cdot \left[\frac{d}{dx} \left(h \frac{\partial \vec{F}}{\partial \vec{U}}\ \vec{u} \right) \right] dx \\ & - \int_D \vec{\nu}^T \cdot \left[\frac{d}{dx} \left(h \frac{d}{dx} \left(\frac{\partial \vec{F}_{v,1}}{\partial \vec{U}}\ \vec{u} \right) \right) \right] dx \\ & - \int_D \vec{\nu}^T \cdot \left[\frac{dh}{dx} \frac{d}{dx} \left(\frac{\partial \vec{F}_{v,2}}{\partial \vec{U}}\ \vec{u} \right) \right]\ dx \\ & + \int_D \vec{\nu}^T \cdot \frac{dh}{dx}\ \frac{\partial \vec{P}}{\partial \vec{U}}\ \vec{u}\ dx \\ & + \int_D \left(\frac{\partial p}{\partial \vec{U}} \right)^T \cdot \vec{u}\ dx \end{aligned} \tag{45}$$

$$\begin{aligned} \Rightarrow I \quad = \quad & \int_D \vec{\nu}^T \cdot \vec{f}\ dx \\ & - \left[\vec{\nu}^T \cdot (h \boldsymbol{A}\ \vec{u}) \right]_{x=x_{inlet}}^{x=x_{outlet}} - \left[\vec{\nu}^T \cdot \left(h \frac{d}{dx} \left(\boldsymbol{C}_1\ \vec{u} \right) \right) \right]_{x=x_{inlet}}^{x=x_{outlet}} + \left[\frac{d\vec{\nu}^T}{dx} \cdot (h\ \boldsymbol{C}_1\ \vec{u}) \right]_{x=x_{inlet}}^{x=x_{outlet}} \\ & - \left[\left(\frac{dh}{dx} \vec{\nu} \right)^T \cdot (\boldsymbol{C}_2\ \vec{u}) \right]_{x=x_{inlet}}^{x=x_{outlet}} \\ & - \int_D \vec{u}^T \cdot \underbrace{\left(- h \boldsymbol{A}^T \frac{d\vec{\nu}}{dx} + \boldsymbol{C}_1^T \frac{d}{dx} \left(h\ \frac{d\vec{\nu}}{dx} \right) - \boldsymbol{C}_2^T\ \frac{d}{dx} \left(\frac{dh}{dx} \vec{\nu} \right)\ -\ \frac{dh}{dx}\ \boldsymbol{B}^T \vec{\nu}\ -\ \frac{\partial p}{\partial \vec{U}} \right)}_{\substack{\boldsymbol{L}^\dagger \vec{\nu} = \vec{g} \\ \textit{The adjoint equations}}} dx. \end{aligned} \tag{46}$$

Viscous linear adjoint solutions $\vec{\nu}(x)$ corresponding to the gradient $\vec{g}(x) = \frac{\partial p}{\partial \vec{U}}$

The adjoint basis solutions can be computed by starting with equation (42), which represents the linearized objective function, the impulse forcing ($\vec{f}(\xi)$) such that

$$\boldsymbol{L}_{viscous}\ \vec{u}(x, \xi) = \vec{f}(\xi) \delta(x - \xi), \tag{47}$$

which is different from the forcing ($\vec{f}_j(\xi)$) which only satisfies

$$\int_D \boldsymbol{L}_{viscous}\ \vec{u}_j(x, \xi)\ d\xi = \int_D \delta(x - \xi)\ \vec{f}_j(\xi)\ d\xi, \tag{48}$$

and response ($\vec{u}(x, \xi)$), we have

$$dJ = I = \int_D \left(\frac{\partial p}{\partial \vec{U}} \right)^T \cdot \vec{u}(x, \xi)\ dx - \int_D \vec{\nu}^T \cdot \Big(\ \boldsymbol{L}_{viscous}\ \vec{u}(x, \xi) - \vec{f}(\xi) \delta(x - \xi)\ \Big)\, dx. \tag{49}$$

Next, equation (49) can be transformed to a form similar to (46) as shown below, using an integration by parts procedure and preserving the terms $\vec{u}(x,\xi)$ or $\vec{f}(\xi)\delta(x-\xi)$ throughout this procedure

$$
\begin{aligned}
I(\xi) \;=\; & \int_D \vec{\nu}^T(x)\cdot\vec{f}(\xi)\delta(x-\xi)\;dx \\
& -\Big[\vec{\nu}^T(x)\cdot\left(h\boldsymbol{A}\;\vec{u}(x,\xi)\right)\Big]_{x=x_{inlet}}^{x=x_{outlet}} - \left[\vec{\nu}^T(x)\cdot\left(h\frac{d}{dx}\left(\boldsymbol{C}_1\;\vec{u}(x,\xi)\right)\right)\right]_{x=x_{inlet}}^{x=x_{outlet}} \\
& +\left[\frac{d\vec{\nu}^T(x)}{dx}\cdot\left(h\;\boldsymbol{C}_1\;\vec{u}(x,\xi)\right)\right]_{x=x_{inlet}}^{x=x_{outlet}} - \left[\left(\frac{dh}{dx}\vec{\nu}(x)\right)^T\cdot\left(\boldsymbol{C}_2\;\vec{u}(x,\xi)\right)\right]_{x=x_{inlet}}^{x=x_{outlet}} \\
& -\int_D \vec{u}^T(x,\xi)\cdot\left(\boldsymbol{L}^\dagger\vec{\nu}-\vec{g}\right)\;dx,
\end{aligned}
\tag{50}
$$

assuming $\boldsymbol{L}^\dagger\vec{\nu}-\vec{g}=\vec{0}$ and that these solutions satisfy the adjoint boundary conditions, then together with equation (47) we have

$$
I(\xi) \;=\; \int_D \vec{\nu}^T(x)\cdot\left\{\boldsymbol{L}_{viscous}\;\vec{u}(x,\xi)\right\}\;dx, \tag{51}
$$

$$
\begin{aligned}
= & \left\{\vec{\nu}^T(x)\cdot\left(h(x)\;\boldsymbol{A}\;\hat{u}_1(x)\right)\;+\;\vec{\nu}^T(x)\cdot\left(h(x)\;\frac{d}{dx}\left(\boldsymbol{C}_1\;\hat{u}_1(x)\right)\right)\right. \\
& \left.\left.+\;\vec{\nu}^T(x)\cdot\left(\frac{dh(x)}{dx}\;\boldsymbol{C}_2\;\hat{u}_1(x)\right)-\frac{d\vec{\nu}^T(x)}{dx}\cdot\left(h(x)\;\boldsymbol{C}_1\;\hat{u}_1(x)\right)\right\}\right|_{x=\xi},
\end{aligned}
\tag{52}
$$

where the solution $\vec{u}(x,\xi)$ is assumed to have the form $H(x-\xi)\hat{u}_1(x)+\hat{u}_2(x)$ and both $\hat{u}_{i=1,2}$ are homogeneous solutions that satisfy $\boldsymbol{L}_{viscous}\hat{u}_i=\vec{0}$. Furthermore, assuming that the boundary conditions are satisfied for all ξ (on account of the properly constructed solutions $\vec{u}(x,\xi)$), we have

$$
I(\xi)=\vec{\nu}^T(\xi)\cdot\left(h(\xi)\;\boldsymbol{A}\;\hat{u}_1(\xi)\;+\;h(\xi)\;\frac{d}{d\xi}\left(\boldsymbol{C}_1\;\hat{u}_1(\xi)\right)\;+\;\frac{dh(\xi)}{d\xi}\;\boldsymbol{C}_2\;\hat{u}_1(\xi)\right)-\frac{d\vec{\nu}^T(\xi)}{d\xi}\cdot\left(h(\xi)\;\boldsymbol{C}_1\;\hat{u}_1(\xi)\right). \tag{53}
$$

Viscous adjoint Green's function operator $\boldsymbol{G}^\dagger_{viscous}(x,\eta)$

Starting with equation (53) from the previous section we have

$$
\begin{aligned}
\int_D\left\{\vec{g}_i^T(\eta)\;\delta(x-\eta)\right\}\cdot\vec{u}(x,\xi)\;dx \;=\; & \vec{\nu}_i^T(\xi,\eta)\cdot\left(h(\xi)\;\boldsymbol{A}\;\hat{u}_1(\xi)\;+\;h(\xi)\;\frac{d}{d\xi}\left(\boldsymbol{C}_1\;\hat{u}_1(\xi)\right)\;+\;\frac{dh(\xi)}{d\xi}\;\boldsymbol{C}_2\;\hat{u}_1(\xi)\right) \\
& -\frac{\partial\vec{\nu}_i^T(\xi,\eta)}{\partial\xi}\cdot\left(h(\xi)\;\boldsymbol{C}_1\;\hat{u}_1(\xi)\right).
\end{aligned}
\tag{54}
$$

$$
\begin{aligned}
\Rightarrow\vec{g}_i^T(\eta)\cdot\vec{u}(\eta,\xi) \;=\; & \vec{\nu}_i^T(\xi,\eta)\cdot\left(h(\xi)\;\boldsymbol{A}\;\hat{u}_1(\xi)\;+\;h(\xi)\;\frac{d}{d\xi}\left(\boldsymbol{C}_1\;\hat{u}_1(\xi)\right)\;+\;\frac{dh(\xi)}{d\xi}\;\boldsymbol{C}_2\;\hat{u}_1(\xi)\right) \\
& -\frac{\partial\vec{\nu}_i^T(\xi,\eta)}{\partial\xi}\cdot\left(h(\xi)\;\boldsymbol{C}_1\;\hat{u}_1(\xi)\right).
\end{aligned}
\tag{55}
$$

Now, replacing the variable ξ with x we have

$$
\Rightarrow\vec{g}_i^T(\eta)\cdot\vec{u}(\eta,x) \;=\; \vec{\nu}_i^T(x,\eta)\cdot\left(h(x)\;\boldsymbol{A}\;\hat{u}(x)\;+\;h(x)\;\frac{d}{dx}\left(\boldsymbol{C}_1\;\hat{u}(x)\right)\;+\;\frac{dh(x)}{dx}\;\boldsymbol{C}_2\;\hat{u}(x)\right)
$$

$$- \frac{\partial \vec{\nu}_i^T(x,\eta)}{\partial x} \cdot \left(h(x)\ \boldsymbol{C}_1\ \hat{u}(x)\right). \tag{56}$$

Upon solving the above partial differential equation for $\vec{\nu}_i(x,\eta)$ for a given gradient $\vec{g}_i(\eta)$, the viscous adjoint Green's function operator $\boldsymbol{G}_s^\dagger(x,\eta)$ can be computed as follows, similar to equation (28)

$$\boldsymbol{G}_s^\dagger(x,\eta) = \left(\vec{v}_1(x,\eta) \mid \vec{v}_2(x,\eta) \mid \vec{v}_3(x,\eta)\right)\ \left(\vec{g}_1(\eta) \mid \vec{g}_2(\eta) \mid \vec{g}_3(\eta)\right)^{-1}. \tag{57}$$

Viscous forward Green's function operator $\boldsymbol{G}_{viscous}(x,\xi)$

Starting with the equation (51) and whilst considering a forward solutions $\tilde{u}_i(x,\xi))$ such that $\boldsymbol{L}_{viscous}\tilde{u}_i(x,\xi)) = \vec{f}_i(\xi)$, we have

$$\int_D \delta(x-\eta)\vec{g}^T(\eta)\cdot\tilde{u}(x,\xi)dx = \int_D \vec{\nu}_j^T(x,\eta)\cdot(\boldsymbol{L}_{viscous}\cdot\tilde{u}(x,\xi))dx, \tag{58}$$

$$\Rightarrow \tilde{u}_i(x,\xi) = (\vec{g}_1(x),\vec{g}_2(x),\vec{g}_3(x))^{-T}\cdot(\vec{\nu}_1(x,\xi),\vec{\nu}_2(x,\xi),\vec{\nu}_3(x,\xi))^T\cdot\vec{f}_i(\xi). \tag{59}$$

Next, three linearly independent vectors $\vec{f}_i(\xi)$ must be computed. This can be accomplished by considering the basis vectors $\vec{u}_i(x,\xi)$ and evaluating the following equations to compute the corresponding $\vec{f}_i(\xi)$ as shown below

$$\begin{aligned}
\vec{f}_j(x) &= \int_D \boldsymbol{L}_{viscous}\vec{u}_j(x,\xi)\ d\xi \\
&= \int_D \left\{ \frac{d}{dx}\left(h\frac{\partial\vec{F}}{\partial\vec{U}}\vec{u}_j(x,\xi)\right) + \frac{d}{dx}\left(h\frac{d}{dx}\left(\frac{\partial\vec{F}_{v,1}}{\partial\vec{U}}\vec{u}_j(x,\xi)\right)\right) + \frac{dh}{dx}\frac{d}{dx}\left(\frac{\partial\vec{F}_{v,2}}{\partial\vec{U}}\ \vec{u}_j(x,\xi)\right) - \frac{dh}{dx}\frac{\partial\vec{P}}{\partial\vec{U}}\vec{u}_j(x,\xi)\right\} d\xi \\
&= \int_D \left\{ H(x-\xi)\ \frac{d}{dx}\left(h(x)\ \frac{\partial\vec{F}}{\partial\vec{U}}\vec{u}_j(x)\right) + \frac{dH(x-\xi)}{dx}\left(h(x)\ \frac{\partial\vec{F}}{\partial\vec{U}}\vec{u}_j(x)\right)\right. \\
&\quad + \frac{d}{dx}\left[h(x)\ H(x-\xi)\ \frac{d}{dx}\left(\frac{\partial\vec{F}_{v,1}}{\partial\vec{U}}\vec{u}_j(x)\right) + h(x)\ \frac{dH(x-\xi)}{dx}\ \left(\frac{\partial\vec{F}_{v,1}}{\partial\vec{U}}\vec{u}_j(x)\right)\right] \\
&\quad \left. + H(x-\xi)\ \frac{dh}{dx}\frac{d}{dx}\left(\frac{\partial\vec{F}_{v,2}}{\partial\vec{U}}\ \vec{u}_j(x)\right) + \frac{dH(x-\xi)}{dx}\ \left(\frac{dh}{dx}\frac{\partial\vec{F}_{v,2}}{\partial\vec{U}}\ \vec{u}_j(x)\right) - H(x-\xi)\ \frac{dh(x)}{dx}\ \frac{\partial\vec{P}}{\partial\vec{U}}\vec{u}_j(x)\right\} d\xi \\
&= \int_D \left\{ H(x-\xi)\ \cancelto{0}{\boldsymbol{L}_{viscous}\vec{u}_j(x)} + \frac{dH(x-\xi)}{dx}\left(h(x)\ \frac{\partial\vec{F}}{\partial\vec{U}}\vec{u}_j(x)\right)\right. \\
&\quad + \frac{dH(x-\xi)}{dx}\ h(x)\ \frac{d}{dx}\left(\frac{\partial\vec{F}_{v,1}}{\partial\vec{U}}\vec{u}_j(x)\right) + \frac{d}{dx}\left[h(x)\ \frac{dH(x-\xi)}{dx}\left(\frac{\partial\vec{F}_{v,1}}{\partial\vec{U}}\vec{u}_j(x)\right)\right] \\
&\quad \left. + \frac{dH(x-\xi)}{dx}\ \left(\frac{dh}{dx}\frac{\partial\vec{F}_{v,2}}{\partial\vec{U}}\ \vec{u}_j(x)\right)\right\} d\xi \\
&= \int_D \left\{ \frac{dH(x-\xi)}{dx}\left(h(x)\ \frac{\partial\vec{F}}{\partial\vec{U}}\vec{u}_j(x)\right) + \frac{dH(x-\xi)}{dx}\ h(x)\ \frac{d}{dx}\left(\frac{\partial\vec{F}_{v,1}}{\partial\vec{U}}\vec{u}_j(x)\right)\right. \\
&\quad \left. + \frac{d}{dx}\left[h(x)\ \frac{dH(x-\xi)}{dx}\ \left(\frac{\partial\vec{F}_{v,1}}{\partial\vec{U}}\vec{u}_j(x)\right)\right] + \frac{dH(x-\xi)}{dx}\ \left(\frac{dh}{dx}\frac{\partial\vec{F}_{v,2}}{\partial\vec{U}}\ \vec{u}_j(x)\right)\right\} d\xi \\
&= \int_D \left\{ \delta(x-\xi)\left(h(x)\ \frac{\partial\vec{F}}{\partial\vec{U}}\vec{u}_j(x)\right) + \delta(x-\xi)\ h(x)\ \frac{d}{dx}\left(\frac{\partial\vec{F}_{v,1}}{\partial\vec{U}}\vec{u}_j(x)\right)\right.
\end{aligned}$$

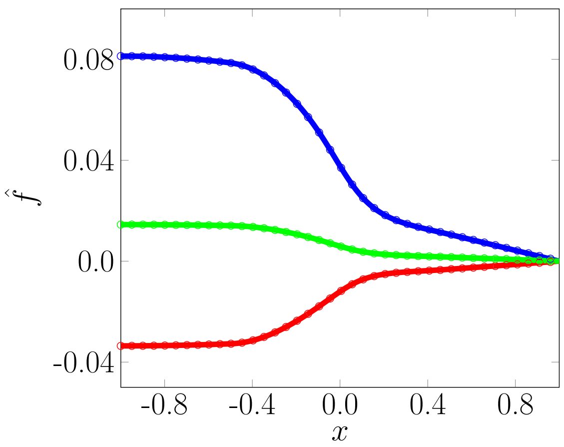

Figure 43: Match between forcing modes computed using as per Giles and Pierce (2001) (solid lines) compared with a central FVM + JST based discrete (circles) implementation for supersonic isentroipic flow through a CD nozzle.

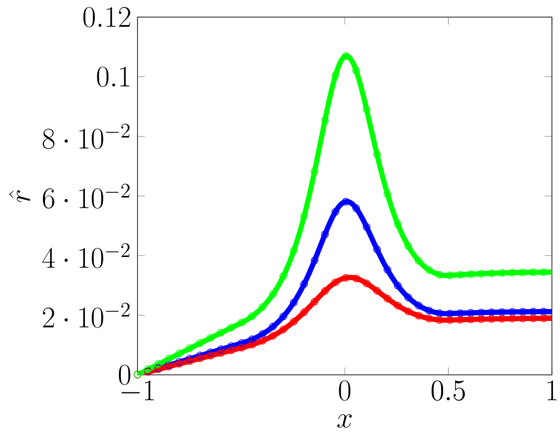

Figure 44: Match between response modes computed using as per Giles and Pierce (2001) (solid lines) compared with a central FVM + JST based discrete (circles) implementation for supersonic isentroipic flow through a CD nozzle.

$$
\begin{aligned}
& +\frac{d}{dx}\left[h(x)\ \delta(x-\xi)\left(\frac{\partial \vec{F}_{v,1}}{\partial \vec{U}}\vec{u}_j(x)\right)\right] +\ \delta(x-\xi)\left(\frac{dh}{dx}\frac{\partial \vec{F}_{v,2}}{\partial \vec{U}}\ \vec{u}_j(x)\right)\Bigg\}\ d\xi \\
= \quad & h(\xi)\ \frac{\partial \vec{F}}{\partial \vec{U}}\vec{u}_j(\xi) + \left\{h(x)\ \frac{d}{dx}\left(\frac{\partial \vec{F}_{v,1}}{\partial \vec{U}}\vec{u}_j(x)\right)\right\}\Bigg|_{x=\xi} + \left\{\frac{dh}{dx}\left(\frac{\partial \vec{F}_{v,2}}{\partial \vec{U}}\vec{u}_j(x)\right)\right\}\Bigg|_{x=\xi} \\
& +\frac{d}{dx}\left[h(x)\ \cancelto{1}{\int_D \delta(x-\xi)d\xi}\left(\frac{\partial \vec{F}_{v,1}}{\partial \vec{U}}\vec{u}_j(x)\right)\right] \\
\Rightarrow \vec{f}_j(x) \quad = \quad & h(x)\ \frac{\partial \vec{F}}{\partial \vec{U}}\vec{u}_j(x) + h(x)\ \frac{d}{dx}\left(\frac{\partial \vec{F}_{v,1}}{\partial \vec{U}}\vec{u}_j(x)\right) + \frac{d}{dx}\left[h(x)\ \left(\frac{\partial \vec{F}_{v,1}}{\partial \vec{U}}\vec{u}_j(x)\right)\right] + \frac{dh}{dx}\left(\frac{\partial \vec{F}_{v,2}}{\partial \vec{U}}\vec{u}_j(x)\right).
\end{aligned}
$$

The viscous forward Green's function operator can now be constructed as follows

$$
\boldsymbol{G}_{viscous}(x,\xi) = (\tilde{u}_1(x,\xi), \tilde{u}_2(x,\xi), \tilde{u}_3(x,\xi)) \cdot (\vec{f}_1(\xi), \vec{f}_2(\xi), \vec{f}_3(\xi))^{-1}. \tag{60}
$$

Resolvent modes corresponding to viscous shock-laden base-flows

Similar to the inviscid case, the zero-frequency resolvent ($\boldsymbol{R}(\omega = 0)$) modes corresponding to the shock-laden flows are computed by solving the eigenvalue problem that originates when computing the SVD of the resolvent operator, given by

$$
\boldsymbol{R}^H(\omega = 0)\ \boldsymbol{R}(\omega = 0)\ \vec{f} = \boldsymbol{G}^{\dagger}_{viscous} * \boldsymbol{G}_{viscous} * \vec{f} = \sigma^2 \vec{f}, \tag{61}
$$

(here $*$ represents the convolution operation), and are in agreement, as shown in Figs. 51 & 51, with the results of the resolvent analysis procedure described in sections 4.2 and 4.4.3.

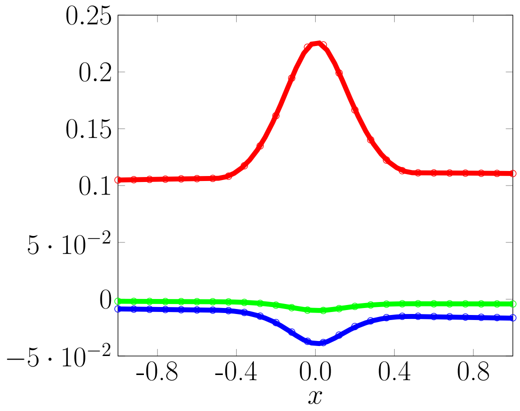

Figure 45: Match between forcing modes computed using as per Giles and Pierce (2001) (solid lines) compared with a central FVM + JST based discrete (circles) implementation for subsonic isentroipic flow through a CD nozzle.

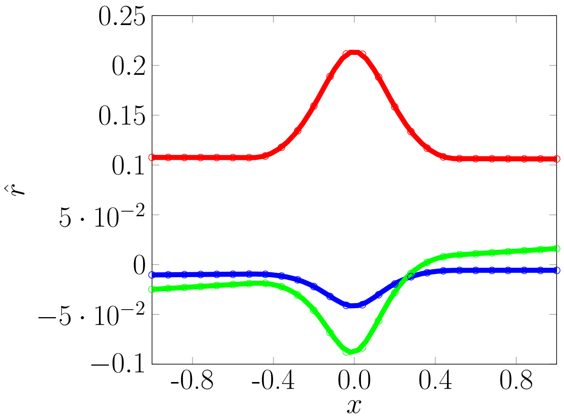

Figure 46: Match between response modes computed using as per Giles and Pierce (2001) (solid lines) compared with a central FVM + JST based discrete (circles) implementation for subsonic isentroipic flow through a CD nozzle.

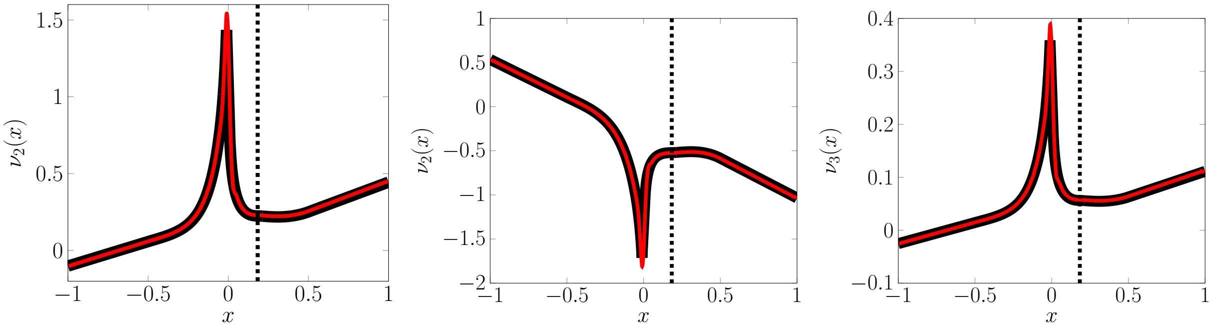

Figure 47: Converged adjoint mode solution (FVM + JST based implementation, represented as ▬) and solution as per Giles and Pierce (2001) , (represented as ▬), corresponding to the transonic shock-laden flow through a quasi 1d model of flow through a CD nozzle.

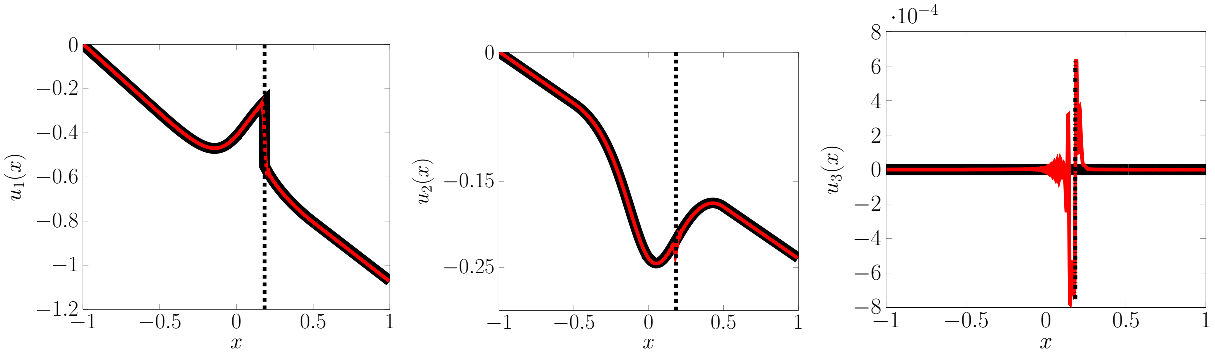

Figure 48: Pointwise converged (except at $x = x_s$) forward mode solution (FVM + JST based implementation represented as 🟥 and solution as per Giles and Pierce (2001) represented as ⬛), corresponding to the transonic shock-laden flow through a quasi 1d model of flow through a CD nozzle.

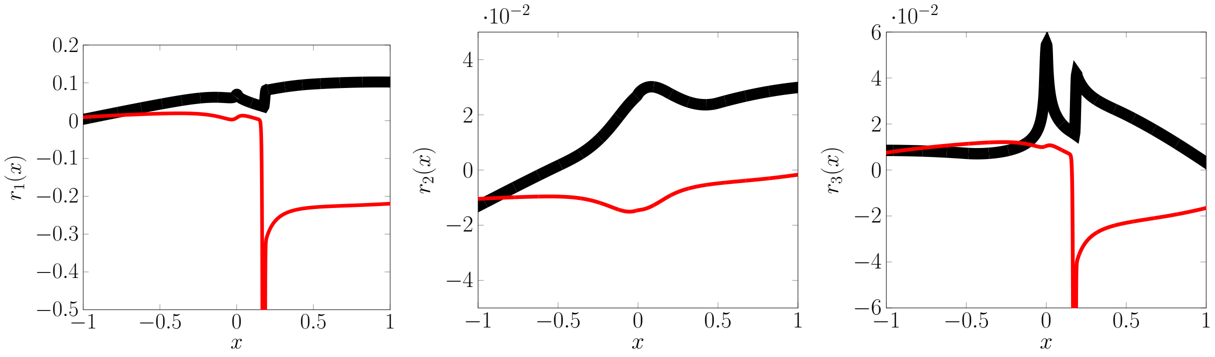

Figure 49: Figure shows a comparison between the resolvent modes computed using equation (30) (represented as 🟥) and using a FVM+viscous-dissipation based implementation (represented as ⬛).

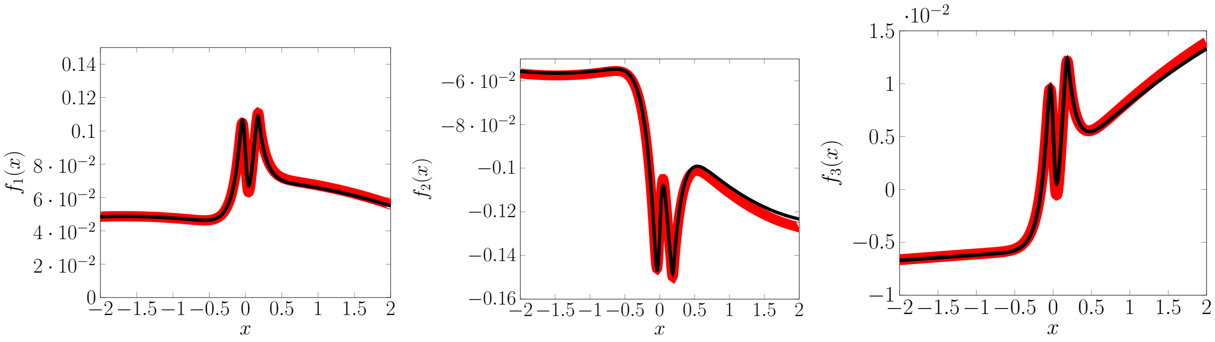

Figure 50: Converged resolvent forcing mode solution (FVM + JST based implementation, represented as 🟥) and solution as per the viscous extension of Giles and Pierce (2001) , (represented as ⬛), corresponding to the transonic shock-laden flow through a quasi 1d model of flow through a CD nozzle.

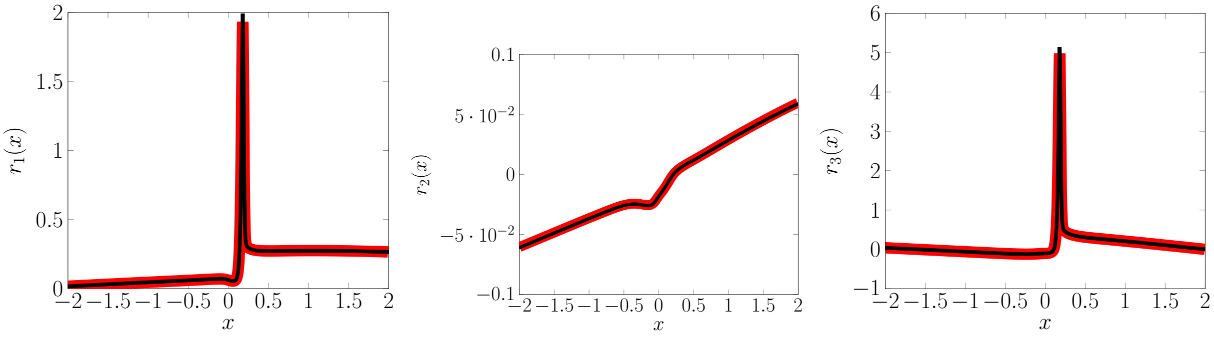

Figure 51: Converged resolvent response mode solution (FVM + JST based implementation, represented as 🟥) and solution as per the viscous extension of Giles and Pierce (2001) , (represented as ⬛), corresponding to the transonic shock-laden flow through a quasi 1d model of flow through a CD nozzle.

6 Conclusion

The reduction of jet noise is a long sought-after goal and significant progress for subsonic jet JNR has been made through a wavepacket–resolvent approach. When applied to supersonic jets, the presence of shocks at under- or overexpanded conditions introduces discontinuities in the flow and numerical method requirements that may corrupt a linearized analysis. In this paper, we examine use the inviscid Burgers' and Euler equations as shock-laden jet surrogates to determine (a) suitable numerical methods whose linearization yields meaningful forward and adjoint sensitivities (and, consequently, meaningful resolvents) and (b) develop semi-analytical results suitable to verifying such methods. Our analysis shows that MUSCL, WENO, or any other method with stencil switching and/or flux limiting is not suitable for linearized analysis despite being appropriate for the forward solution. Localized artificial diffusivity methods are shown to work. Using the quasi-one-dimensional Euler equations, we developed a semi-analytical theory to verify these claims and preliminary results were presented. We show in particular that although forward and adjoint Green's functions provide convergent results when shocks are present, the zero-frequency resolvent modes do not yet converge when constructed as the product of the adjoint and forward operators that separately demonstrate pointwise convergence (except at the shock) to the solutions. This issue will be the topic of future work.

References

Beneddine, S., Sipp, D., Arnault, A., Dandois, J., and Lesshafft, L. (2016). Conditions for validity of mean flow stability analysis. *Journal of Fluid Mechanics*, 798:485–504.

Bodony, D. and Natarajan, M. (2012). Controller selection and placement in compressible turbulent flows. In *Proceedings of the Summer Program*, pages 35–42. Center for Turbulence Research.

Bodony, D. J. and Fikl, A. (2022). Adjoint-based sensitivity of shock-laden flows. Proceedings of the 2022 Summer Program, Center for Turbulence Research.

Bodony, D. J., Zagaris, G., Reichert, A., and Zhang, Q. (2011). Provably stable overset grid methods for computational aeroacoustics. *Journal of Sound and Vibration*, 330:4161–4179.

Bogey, C. and Bailly, C. (2004). A family of low dispersive and low dissipative explicit schemes for flow and noise computations. *Journal of Computational physics*, 194(1):194–214.

Brandt, L., Sipp, D., Pralits, J. O., and Marquet, O. (2011). Effect of base-flow variation in noise amplifiers: the flat-plate boundary layer. *Journal of Fluid Mechanics*, 687:503–528.

Bridges, J. and Brown, C. (2004). Parametric testing of chevrons on single flow hot jets. AIAA Paper 2004-2824, Presented at the 10th AIAA/CEAS Aeroacoustics Conference, Manchester, GREAT BRITAIN.

Chomaz, J.-M. (2005). Global instabilities in spatially developing flows: non-normality and nonlinearity. *Annual Review of Fluid Mechanics*, 37:357–392.

Comte-Bellot, G. and Corrsin, S. (1971). Simple eulerian time correlation of full-and narrow-band velocity signals in grid-generated,'isotropic'turbulence. *Journal of fluid mechanics*, 48(2):273–337.

Crighton, D. and Gaster, M. (1976). Stability of slowly diverging jet flow. *Journal of Fluid Mechanics*, 77(2):397–413.

de Pando, M. F., Schmid, P., and Lele, S. (2014). Parametric sensitivity for large-scale aeroacoustic flows. In *Proceedings of the Summer Program*, page 365.

Diener, M., Bodony, D. J., and Kale, L. (2019). Accelerating scientific applications on heterogeneous systems with hybridomp. In *High Performance Computing for Computational Science–VECPAR 2018: 13th International Conference, São Pedro, Brazil, September 17-19, 2018, Revised Selected Papers 13*, pages 174–187. Springer.

Diener, M., Kale, L. V., and Bodony, D. J. (2020). Heterogeneous computing with openmp and hydra. *Concurrency and Computation: Practice and Experience*, 32(20):e5728.

Diener, M., White, S., Kale, L. V., Campbell, M., Bodony, D. J., and Freund, J. B. (2017). Improving the memory access locality of hybrid mpi applications. In *Proceedings of the 24th European MPI Users' Group Meeting*, pages 1–10.

Farrell, B. F. and Ioannou, P. J. (1993). Stochastic forcing of the linearized navier–stokes equations. *Physics of Fluids A: Fluid Dynamics*, 5(11):2600–2609.

Farrell, B. F. and Ioannou, P. J. (1996). Generalized stability theory. part i: Autonomous operators. *Journal of Atmospheric Sciences*, 53(14):2025–2040.

Farrell, B. F. and Ioannou, P. J. (2019). Statistical state dynamics: A new perspective on turbulence in shear flow. *Zonal Jets Phenomenology, Genesis, and Physics.*, pages 380–400.

Garnaud, X., Lesshafft, L., Schmid, P., and Huerre, P. (2013). The preferred mode of incompressible jets: linear frequency response analysis. *Journal of Fluid Mechanics*, 716:189–202.

Germano, M., Piomelli, U., Moin, P., and Cabot, W. H. (1991). A dynamic subgrid-scale eddy viscosity model. *Physics of Fluids A: Fluid Dynamics*, 3(7):1760–1765.

Giles, M., Pierce, N., Giles, M., and Pierce, N. (1997). Adjoint equations in cfd-duality, boundary conditions and solution behaviour. In *13th computational fluid dynamics conference*, page 1850.

Giles, M. B. and Pierce, N. A. (2001). Analytic adjoint solutions for the quasi-one-dimensional euler equations. *Journal of Fluid Mechanics*, 426:327–345.

Goldstein, M. E. (2003). A generalized acoustic analogy. *Journal of Fluid Mechanics*, 488:315–333.

Gudmundsson, K. and Colonius, T. (2011). Instability wave models for the near-field fluctuations of turbulent jets. *Journal of Fluid Mechanics*, 689:97–128.

Jameson, A., Schmidt, W., and Turkel, E. (1981). Numerical solution of the euler equations by finite volume methods using runge-kutta time-stepping schemes. AIAA Paper 81-1259, Presented at the 14th AIAA Fluid and Plasma Dynamics Conference Palo Alto, CA, 23–25 May.

Jeun, J., Nichols, J. W., and Jovanović, M. R. (2016). Input-output analysis of high-speed axisymmetric isothermal jet noise. *Physics of Fluids*, 28(4):047101.

Jiang, G.-S. and Shu, C.-W. (1996). Efficient implementation of weighted eno schemes. *Journal of computational physics*, 126(1):202–228.

Jordan, P. and Colonius, T. (2013). Wave packets and turbulent jet noise. *Annual Review of Fluid Mechanics*, 45:173–195.

Jovanović, M. R. and Bamieh, B. (2005). Componentwise energy amplification in channel flows. *Journal of Fluid Mechanics*, 534:145–183.

Kawai, S. and Lele, S. K. (2008). Localized artificial diffusivity scheme for discontinuity capturing on curvilinear meshes. *Journal of Computational Physics*, 227:9498—9526.

Kim, J., Bodony, D. J., and Freund, J. B. (2014). Adjoint-based control of loud events in a turbulent jet. *Journal of Fluid Mechanics*, 741:28–59.

Lele, S. K. (1992). Compact finite difference schemes with spectral-like resolution. *Journal of computational physics*, 103(1):16–42.

Lesshafft, L., Semeraro, O., Jaunet, V., Cavalieri, A. V., and Jordan, P. (2019). Resolvent-based modeling of coherent wave packets in a turbulent jet. *Physical Review Fluids*, 4(6):063901.

Leveque, R. J. (2002). *Finite Volume Methods for Hyperbolic Problems.* Cambridge Texts in Applied Mathematics. Cambridge Univ. Press.

Li, Z., Ju, Y., and Zhang, C. (2017). Hybrid central–weno scheme for the large eddy simulation of turbulent flows with shocks. *Numerical Heat Transfer, Part B: Fundamentals*, 72(2):170–189.

Liu, J. and Corrigan, A. T. (2018). Large-eddy simulations of supersonic jet noise generation using wall modeling. In *2018 AIAA/CEAS Aeroacoustics Conference*, page 3943.

Liu, J., Corrigan, A. T., Kailasanath, K., Heeb, N. S., Munday, D. E., and Gutmark, E. J. (2013). Computational study of shock-associated noise characteristics using les. In *19th AIAA/CEAS Aeroacoustics Conference*, page 2199.

Liu, J., Corrigan, A. T., Kailasanath, K., and Taylor, B. D. (2016). Impact of the specific heat ratio on the noise generation in a high-temperature supersonic jet. In *54th AIAA Aerospace Sciences Meeting*, page 2125.

Liu, J., Kailasanath, K., and Gutmark, E. J. (2017). Similarity spectra analysis in highly heated supersonic jets using large-eddy simulations. In *55th AIAA Aerospace Sciences Meeting*, page 0926.

Liu, Q., Sun, Y., Yeh, C.-A., Ukeiley, L. S., Cattafesta, L. N., and Taira, K. (2021). Unsteady control of supersonic turbulent cavity flow based on resolvent analysis. *Journal of Fluid Mechanics*, 925:A5.

Martín, M. P., Taylor, E. M., Wu, M., and Weirs, V. G. (2006). A bandwidth-optimized weno scheme for the effective direct numerical simulation of compressible turbulence. *Journal of Computational Physics*, 220(1):270–289.

Mendez, S., Shoeybi, M., Sharma, A., Lele, S., and Moin, P. (2009). Post-processing of large-eddy simulations for jet noise predictions. *Center for Turbulence Research Annular Research Briefs*, pages 17–31.

Michalke, A. (1977). Instability of a compressible circular free jet with consideration of the influence of the jet boundary layer thickness.

Moin, P., Squires, K., Cabot, W., and Lee, S. (1991). A dynamic subgrid-scale model for compressible turbulence and scalar transport. *Physics of Fluids A: Fluid Dynamics*, 3(11):2746–2757.

Munday, D., Gutmark, E., Liu, J., and Kailasanath, K. (2011). Flow structure and acoustics of supersonic jets from conical convergent-divergent nozzles. *Physics of Fluids*, 23(11).

Murthy, S. R. and Bodony, D. J. (2022). Resolvent analysis of a biconical tactical jet nozzle. In *28th AIAA/CEAS Aeroacoustics 2022 Conference*, page 2969.

Natarajan, M. (2017). *Actuator selection and placement for linear feedback control of compressible flows*. PhD thesis, University of Illinois at Urbana-Champaign.

Natarajan, M., Freund, J. B., and Bodony, D. J. (2016a). Actuator selection and placement for localized feedback flow control. *Journal of Fluid Mechanics*, 809:775–792.

Natarajan, M., Freund, J. B., and Bodony, D. J. (2016b). Actuator selection and placement for localized feedback flow control. *Journal of Fluid Mechanics*, 809:775–792.

Nonomura, T., Terakado, D., Abe, Y., and Fujii, K. (2015). A new technique for freestream preservation of finite-difference weno on curvilinear grid. *Computers & Fluids*, 107:242–255.

Norum, T. and Seiner, J. (1982). Broadband shock noise from supersonic jets. *AIAA Journal*, 20(1):68–73.

Ponton, M. and Seiner, J. (1992). The effects of nozzle exit lip thickness on plume resonance. *Journal of Sound and Vibration*, 154(3):531–549.

Schmid, P. J. (2007). Nonmodal stability theory. *Annual Review of Fluid Mechanics*, 39:129–162.

Schmid, P. J., Henningson, D. S., and Jankowski, D. (2002). Stability and transition in shear flows. applied mathematical sciences, vol. 142. *Appl. Mech. Rev.*, 55(3):B57–B59.

Seiner, J., Ukeiley, L., Jansen, B., Kannepalli, C., and Dash, S. (2004). Noise reduction technology for F/A-18 E/F aircraft. AIAA Paper 2004-2972, Presented at the 10th AIAA/CEAS Aeroacoustics Conference, Manchester, GREAT BRITAIN.

Sipp, D. and Marquet, O. (2013). Characterization of noise amplifiers with global singular modes: the case of the leading-edge flat-plate boundary layer. *Theoretical and Computational Fluid Dynamics*, 27(5):617–635.

Visbal, M. R. and Gaitonde, D. V. (2002). On the use of higher-order finite-difference schemes on curvilinear and deforming meshes. *Journal of Computational Physics*, 181(1):155–185.

Williams, J. F. and Maidanik, G. (1965). The mach wave field radiated by supersonic turbulent shear flows. *Journal of Fluid Mechanics*, 21(4):641–657.

REPORT DOCUMENTATION PAGE

1. REPORT DATE	**2. REPORT TYPE**	**3. DATES COVERED**	
		START DATE	**END DATE**
01/19/2024	Final	06/01/2019	08/31/2023

4. TITLE AND SUBTITLE
Reducing Noise from Single and Twin Supersonic Jets Using Very-Low-Frequency Control

5a. CONTRACT NUMBER	**5b. GRANT NUMBER**	**5c. PROGRAM ELEMENT NUMBER**
N00014-19-1-2431		
5d. PROJECT NUMBER	**5e. TASK NUMBER**	**5f. WORK UNIT NUMBER**

6. AUTHOR(S)
Bodony, Daniel, J. (PI) and Murthy, Sandeep, R.

7. PERFORMING ORGANIZATION NAME(S) AND ADDRESS(ES)	**8. PERFORMING ORGANIZATION REPORT NUMBER**
University of Illinois at Urbana-Champaign	N/A

9. SPONSORING/MONITORING AGENCY NAME(S) AND ADDRESS(ES)	**10. SPONSOR/MONITOR'S ACRONYM(S)**	**11. SPONSOR/MONITOR'S REPORT NUMBER(S)**
Office of Naval Research 875 N. Randolph Street Suite 1425 Arlington VA 22203-1995	ONR	

12. DISTRIBUTION/AVAILABILITY STATEMENT
Distribution A, Unlimited

13. SUPPLEMENTARY NOTES

14. ABSTRACT
A jet noise reduction (JNR) approach was developed and applied to single and twin supersonic jets issuing from bi-conical converging-diverging nozzles. The JNR approach uses large-eddy simulation (LES) to predict the jet noise, applies an input-output operator-based sensitivity analysis to identify and localize the best JNR strategy, and then tests the JNR strategy in controlled-jet LES. Frequency-specific JNR was observed for jets with shocks of modest strengths. It was found that input-output operators fail when strong shocks are present and, a new mathematical and numerical approach was developed to permit strong shocks, but the project ended before JNR application.

15. SUBJECT TERMS
Jet noise reduction; large eddy simulation

16. SECURITY CLASSIFICATION OF:			**17. LIMITATION OF ABSTRACT**	**18. NUMBER OF PAGES**
a. REPORT	**b. ABSTRACT**	**C. THIS PAGE**		
U	U	U	UU	51

19a. NAME OF RESPONSIBLE PERSON	**19b. PHONE NUMBER** *(Include area code)*
Daniel J. Bodony	(217) 244-3844